

## Age-Depth Stratigraphy of Pine Island Glacier Inferred From Airborne Radar and Ice-Core Chronology

**Key Points:**

- Using airborne radar, we trace four isochronous internal reflecting horizons over Pine Island Glacier, West Antarctica
- Isochrone ages calculated using the WAIS Divide ice core and a 1-D model are 2.31–2.92,  $4.72 \pm 0.28$ ,  $6.94 \pm 0.31$ , and  $16.50 \pm 0.79$  ka
- We show that these isochrones are widespread across Pine Island Glacier and extend into neighboring Weddell and Amundsen Sea regions

**Supporting Information:**

Supporting Information may be found in the online version of this article.




**Correspondence to:**

J. A. Bodart,  
[julien.bodart@ed.ac.uk](mailto:julien.bodart@ed.ac.uk)

**Citation:**

Bodart, J. A., Bingham, R. G., Ashmore, D. W., Karlsson, N. B., Hein, A. S., & Vaughan, D. G. (2021). Age-depth stratigraphy of Pine Island Glacier inferred from airborne radar and ice-core chronology. *Journal of Geophysical Research: Earth Surface*, 126, e2020JF005927. <https://doi.org/10.1029/2020JF005927>

Received 30 SEP 2020  
Accepted 17 MAR 2021

J. A. Bodart<sup>1,4</sup> , R. G. Bingham<sup>1</sup> , D. W. Ashmore<sup>2</sup> , N. B. Karlsson<sup>3</sup> , A. S. Hein<sup>1</sup> , and D. G. Vaughan<sup>4</sup> 

<sup>1</sup>School of GeoSciences, University of Edinburgh, Edinburgh, UK, <sup>2</sup>School of Environmental Sciences, University of Liverpool, Liverpool, UK, <sup>3</sup>Geological Survey of Denmark and Greenland, Copenhagen, Denmark, <sup>4</sup>British Antarctic Survey, Cambridge, UK

**Abstract** Understanding the contribution of the West Antarctic Ice Sheet (WAIS) to past and future sea level has been a major scientific priority over the last three decades. In recent years, observed thinning and ice-flow acceleration of the marine-based Pine Island Glacier has highlighted that understanding dynamic changes is critical to predicting the long-term stability of the WAIS. However, relatively little is known about the evolution of the catchment during the Holocene. Internal reflecting horizons (IRHs) provide a cumulative record of accumulation, basal melt, and ice dynamics that, if dated, can be used to constrain ice-flow models. Here, we use airborne radars to trace four spatially extensive IRHs deposited in the late Quaternary across the Pine Island Glacier catchment. We use the WAIS Divide ice-core chronology to assign ages to three IRHs:  $4.72 \pm 0.28$ ,  $6.94 \pm 0.31$ , and  $16.50 \pm 0.79$  ka. We use a 1-D model, constrained by observational and modeled accumulation rates, to produce an independent validation of our ice-core-derived ages and provide an age estimate for our shallowest IRH (2.31–2.92 ka). We find that our upper three IRHs correspond to three large peaks in sulfate concentrations in the WAIS Divide ice-core record and hypothesize that the origin of these spatially extensive IRHs is from past volcanic activity. The clear correspondence between our IRHs and the ones previously identified over the Weddell Sea Sector, altogether representing ~20% of the WAIS, indicates that a unique set of stratigraphic markers spanning the Holocene exists over a large part of West Antarctica.

### 1. Introduction

The West Antarctic Ice Sheet (WAIS) has been losing mass at an accelerating rate since satellite records began, averaging  $94 \pm 27$  Gt yr<sup>-1</sup> of mass loss since 1992 (Shepherd et al., 2018). Approximately 40% of this loss was through Pine Island Glacier (PIG), which alone has contributed ~3 mm of the total ~7 mm sea-level-rise contribution of the WAIS between 1979 and 2017 (Rignot et al., 2019). The increasing mass-loss trend of PIG has been primarily driven by interannual and decadal-scale atmospheric and oceanic forcing, triggering grounding-line retreat and consequent inland dynamical adjustments (Bodart & Bingham, 2019; Christianson et al., 2016; Dutrieux et al., 2014; Favier et al., 2014; Holland et al., 2019; Konrad et al., 2017; Rignot et al., 2019; Smith et al., 2017). However, placing the observed changes over the last four decades within the context of long-term dynamic changes and sea-level rise contribution is challenging (Medley et al., 2018; Palerme et al., 2017), as the short observational satellite record captures only slight perturbations in the forcing and response which are not sufficient to predict a future in which changes are likely to be rapid and large. This lack of long-term observations currently limits our understanding of the likely future evolution of this sensitive sector of the WAIS. Reaching further back into the past will help us capture a wider set of ice-sheet configurations, and so create a more robust basis for future predictions of the Antarctic Ice Sheet evolution (Bracegirdle et al., 2019; DeConto & Pollard, 2016; Ritz et al., 2001).

Past research has focused primarily on using in situ observations and ice-sheet models to reconstruct the evolution of the WAIS since the Last Glacial Maximum (LGM, ~20 ka BP), indicating that WAIS contained significantly more ice than at present, with the potential to have raised sea level by more than 9 m at the LGM (Denton & Hughes, 2002). Several studies have reported evidence of short-lived episodes of rapid grounding-line retreat in the Amundsen Sea Embayment (ASE) between the LGM and the start of the Holocene (~11.5 ka BP) (Hillenbrand et al., 2013; Jakobsson et al., 2011; Lowe & Anderson, 2002). However, much less is known about the interior ice-sheet history of this region during the Holocene. Cosmogenic

© 2021. The Authors.

This is an open access article under the terms of the [Creative Commons Attribution License](https://creativecommons.org/licenses/by/4.0/), which permits use, distribution and reproduction in any medium, provided the original work is properly cited.

nuclide studies on isolated nunataks across the ASE suggest significant ice thinning occurred during the early- to mid-Holocene in the central ASE (Johnson et al., 2017, 2020; Lindow et al., 2014), with thinning complete by the mid-Holocene in the eastern ASE near PIG (Johnson et al., 2008, 2014). More recent evidence, based on sediment cores, ice-penetrating radar, and ice-sheet modeling, showed possible retreat and re-advance of the WAIS grounding line over millennial timescales during the Holocene (Kingslake et al., 2018), although evidence of such behavior is not available in the ASE region.

Internal reflecting horizons (IRHs), as observed by ice-penetrating radars, provide a powerful and complementary resource to point-based geochronological measurements. Excluding basal ice and erosional surfaces, the majority of specular, continuous IRHs are isochronous (Whillans, 1976); many can be traced for several hundreds of kilometers and provide a record of accumulation rates and patterns, convolved with key information on past ice-dynamical processes (Bingham & Siegert, 2007; Eisen et al., 2005, 2008; Siegert et al., 1998). IRHs can thus serve as a valuable resource for constraining past changes in surface mass balance (SMB) and ice-flow velocities (e.g., Rotschky et al., 2004), and, where they can be dated, can be incorporated into ice-flow models, as previously shown for Greenland (Fahnestock, et al., 2001; MacGregor et al., 2016) and Antarctica (Cavitte et al., 2018; Koutnik et al., 2016; Leysinger Vieli et al., 2011; Waddington et al., 2007).

Despite the large spatial coverage of radar data across Antarctica, information on dated IRHs is limited over much of the WAIS. This is partly due to the restricted availability of deep ice cores, the multitude of radar-system families operating at varying frequencies and using different post-processing methods to generate the radar data, and the challenge in tracing deep continuous IRHs, particularly through areas of high strain rate (i.e., at the onset of fast-flowing tributaries). Nonetheless, previous studies over the WAIS have used IRHs for the direct purpose of linking major deep ice cores (Koutnik et al., 2016; Neumann et al., 2008), while others have used a wider, catchment-scale approach to constrain information on past accumulation rates and ice-flow reconfiguration. Such studies have ranged across the central WAIS (Jacobel & Welch, 2005; Muldoon, 2018; Siegert & Payne, 2004) or focused on specific sub-regions, for example, Siple Dome (Jacobel et al., 1996), Kamb Ice Stream (Catania et al., 2006; Holschuh et al., 2018) and Thwaites Glacier (Muldoon et al., 2018).

Over PIG, Karlsson et al. (2014) identified two IRHs spanning much of the slow-flowing parts of the catchment, which they roughly dated to 5.3–6.2 and 8.6–13.4 ka. More recently, Ashmore et al. (2020) recovered three IRHs ranging across Institute and Möller Ice Streams and crossing the Institute/PIG divide which they broadly dated to 1.9–3.2, 3.5–6.0, and 4.6–8.1 ka. They demonstrated a correspondence between their IRH package and the IRHs previously identified by Karlsson et al. (2014) and Siegert et al. (2005), suggesting that a spatially extensive network of IRHs may span much of the WAIS.

Here, we build on previous studies to present a spatially extensive, dated-radiostratigraphy of PIG. We use ice-penetrating radar data collected from two airborne platforms to trace four IRHs throughout PIG. We use a published ice-core chronology as well as a steady-state vertical-strain model to date these IRHs, and show that they span much of the Late Pleistocene and Holocene. We first discuss the specifications of the radar systems and their respective uncertainties, and then describe the methods used to assign ages to each of our four IRHs. We present the dated age-depth stratigraphy of the catchment and make inferences for the rest of WAIS by comparing our recent findings to other age-depth studies. Finally, we investigate the link between sulfate activity in the WAIS Divide ice-core record and the depth of our upper three IRHs, and discuss the potential to recover records of older (i.e., pre-LGM) ice in the region using currently available radar data sets.

## 2. Data Sets and Methods

### 2.1. Data

The principal data used in this study were acquired during two large-scale airborne radar surveys of West Antarctica.

The first of these was acquired over the 2004–05 austral season, when PIG's 175,000 km<sup>2</sup> catchment was surveyed extensively using the British Antarctic Survey's Polarimetric Airborne Survey INstrument (PASIN)

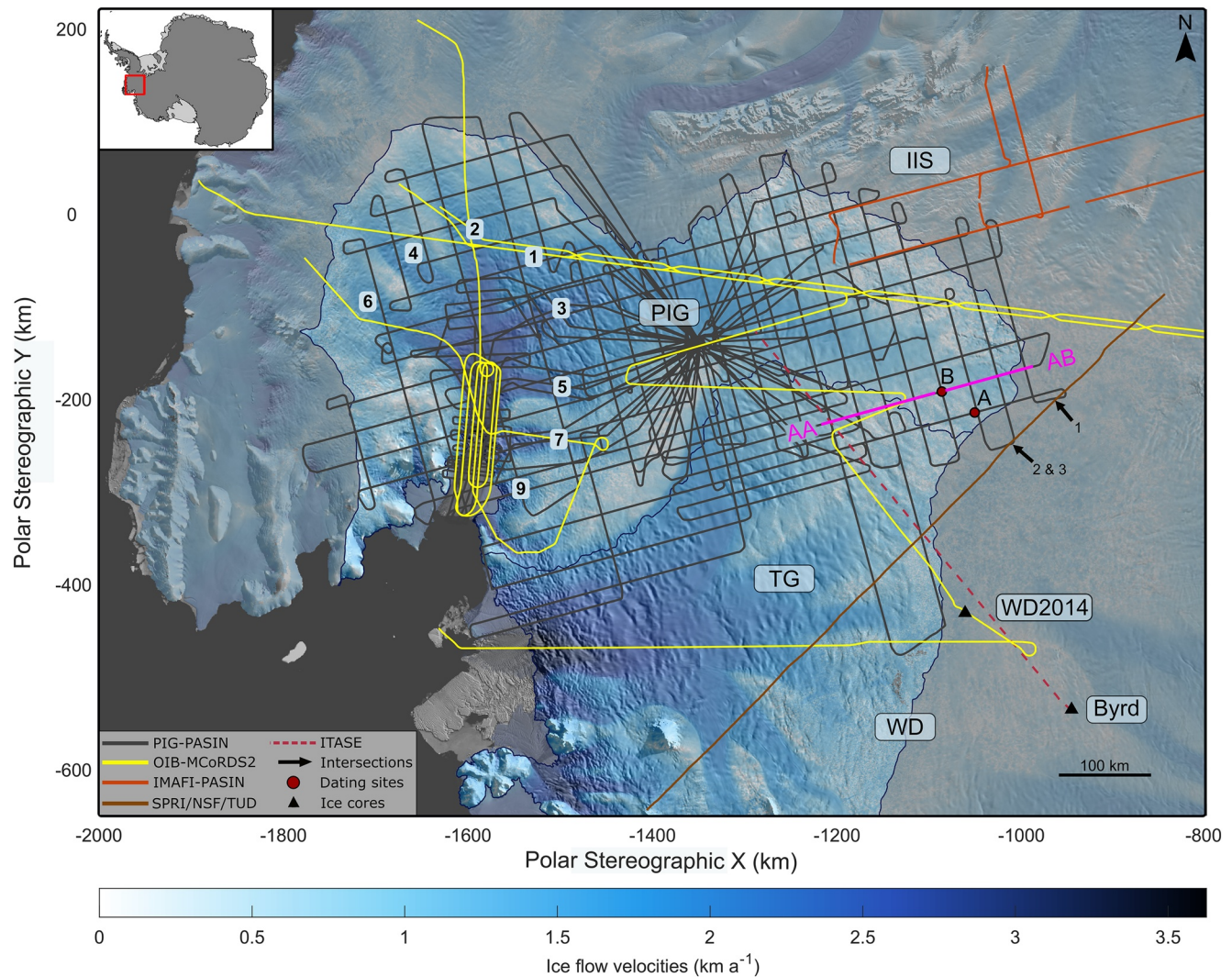


**Figure 1.** Map of study area with the data sets and key locations mentioned in this study. The inset in top left corner shows the region of interest (red box). Airborne survey lines included in this study: PIG-PASIN (gray), OIB-MCoRDS2 (yellow), IMAFI-PASIN transects flown over Institute Ice Stream (IIS) and intersecting the PIG catchment (orange), SPRI/NSF/TUD line (brown), overlaid on top of ice flow velocities from Rignot et al. (2017) and MODIS Mosaic of Antarctica (Scambos et al., 2007). Also included is the long, ITASE GPR-transect (dashed red) through which the  $17.5 \pm 0.5$  ka layer from Jacobel and Welch (2005) was traced. The numbers shown over PIG’s trunk represent the eight fast-flowing tributaries (1–7, 9) mentioned in this study. The WAIS Divide (WD2014) and Byrd ice cores are represented by the two black triangles, and the black arrows represent the three intersections between the SPRI/NSF/TUD-traced IRHs and this study. The two red circles show the two sites (Sites A and B) where the 1-D age-depth model was used. The AA–AB segment (magenta) shows a subset of the control line where IRHs were first identified over PIG-PASIN (see Figure 2). The Western Divide is shown as WD on the map. The ICESat IMBIE basins of Pine Island Glacier (PIG) and Thwaites Glacier (TG) (Zwally et al., 2012) are annotated on the map and delimited by the blue outline lines.

system (Vaughan et al., 2006). This survey, hereafter termed “PIG-PASIN”, acquired  $\sim 35,000$  line-km of airborne radar data across the region (Figure 1). Data were collected with two interleaved radar modes. The first was a deep-sounding, 150 MHz center-frequency,  $4\text{-}\mu\text{s}$ , 10-MHz chirp mode, which has been used previously to identify and trace the bed (Vaughan et al., 2006) and some IRHs (Karlsson et al., 2009, 2014). The second was a 150 MHz,  $0.1\text{-}\mu\text{s}$  pulse mode designed to image shallow IRHs but from which we are also able to recover IRHs deeper ( $\sim 2$  km, see Figure 2a) in the ice column. Over much of the surveyed region, flight lines form 30 km spaced grids that contain multiple crossovers, ensuring consistency when tracing IRHs across neighboring lines (Figure 1). Following techniques outlined in Ashmore et al. (2020), here, we used both modes of PASIN interchangeably during our IRH-tracing procedures (see Section 2.2). For the purposes of linking our stratigraphy further across the WAIS, we also refer to further PASIN-acquired data from a survey of Institute and Möller Ice Streams undertaken in 2010–11 (hereafter “IMAFI-PASIN”),

**Table 1**  
*Characteristics and Resolution of the Two Airborne Radar Systems Used in This Study*

System	Platform	Center frequency	Bandwidth/pulse width	Vertical sampling frequency	Vertical resolution	Horizontal sampling distance
PASIN	Twin Otter	150 MHz	10 MHz/100 ns	22 MHz	12.89/8.42 m	45 m
MCoRDS2	DC8	190 MHz	50 MHz	150 MHz	2.58 m	14 m

*Note:* for the PASIN system, we provide values for both the chirp- and pulse-acquisition mode in the bandwidth/pulse width column, as well as in the vertical resolution column. The vertical resolution of the chirped systems was calculated as per CReSIS (2016) using a scaling factor “*k*” which accounts for resolution degradation due to receiver characteristics and processing (see Equation S1).

which provided tie-lines connecting PIG with its neighboring basins (Figure 1; see Ashmore et al., 2020, and references therein, for further details).

The second survey was conducted in 2016 and 2018 by NASA’s Operation IceBridge (OIB) mission, and yielded ~3,000 line-km of airborne radar data over PIG, Institute and Möller Ice Streams, and Thwaites Glacier (Figure 1). The system deployed by the Center for Remote Sensing of Ice Sheets (CReSIS) was the Multichannel Coherent Radar Depth Sounder 2 (MCoRDS2) with a 190 MHz center frequency and 50 MHz bandwidth. We used the CReSIS L1B standard products, produced with pulse compression, focused-SAR processing, and along-track motion compensation. More information on the radar system and processing is given by CReSIS (2016). Critically for this study, one of the OIB flight tracks over PIG also flew over the WAIS Divide Ice Core (79.48°S, 112.11°W; hereafter referred to as WD2014) (Figure 1), making it possible to assign relatively unambiguous dates to the traced IRHs.

More details on each of the radar systems are provided in Table 1. For the purposes of increasing IRH traceability on the PIG-PASIN data, we quadratically detrended each radar trace, normalized each pixel in a moving vertical window, and then applied a 10-trace horizontal average to reduce incoherent noise (after Ashmore et al., 2020). For both the PIG-PASIN and the OIB-MCoRDS2 data, we removed the air-to-ice two-way travel time and shifted the surface elevation to time zero, before exporting the data to standard 2-D SEG-Y format for data interpretation.

## 2.2. IRH-Tracing Workflow

We conducted all IRH-tracing in the Schlumberger Petrel® 3-D seismic software using a semi-automated tracing algorithm that uses an adjustable window to track the local maxima of received reflected power between traces.

We initiated our workflow on the PIG-PASIN data set as it is the most spatially extensive survey of the PIG catchment. From a “control line” crossing the ice divides between PIG, Thwaites Glacier, and Institute Ice Stream (Figure 1), in which clearly visible englacial stratigraphy is ubiquitous in both chirp- and pulse-mode data, we identified four prominent IRHs that we term R1–4 (Figure 2). The upper three IRHs (R1–3) were chosen on the basis of high spatial continuity, high signal-to-noise ratio (SNR), and as being analogous to “IRH packages” traced over part of PIG by Karlsson et al. (2014) and through IMAFI-PASIN radar profiles by Ashmore et al. (2020). All four IRHs occur in the middle part of the ice column where IRHs likely result from contrasts in acidity from past volcanic eruptions (Gow & Williamson, 1971; Millar, 1981, 1982), rather than the result of density variations occurring primarily at the near-surface (Clough, 1977; Gow, 1970; Moore, 1988) or orientation of anisotropic material due to ice foliation in the basal zone (Fujita et al., 1999; Harrison, 1973); and thus can be assumed to be isochronous (Siegert et al., 1998; Whillans, 1976).

Expanding out from the control line, we progressively traced and mapped IRHs across the catchment using IRH intersections at each crossover as calibration points. This ensured reliability in our reflection tracing as the software is capable of detecting intersecting IRHs at the crossover with orthogonal radar lines. Since our tracing strategy was based on reflector echo strength and continuity, the reflection tracing was terminated when it was no longer possible to distinguish visually between adjacent reflections, either as a result of similar brightness levels or a loss in continuity. This was particularly common in areas of steep bed topography

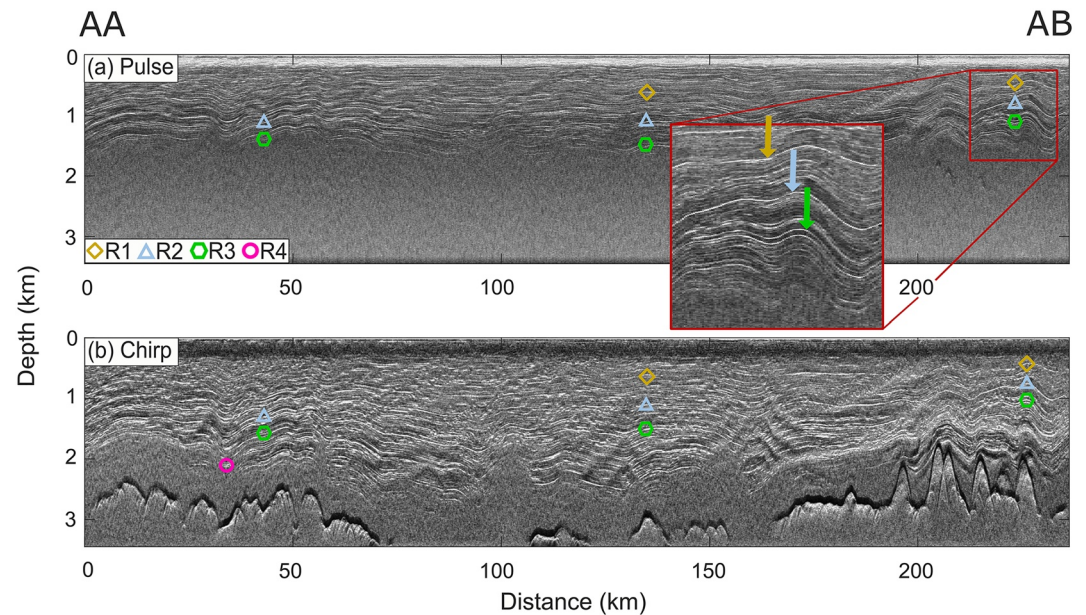


**Figure 2.** Subset of the control line with the unmodulated pulse (a) and chirp (b) modes from the PIG-PASIN survey along transect AA– AB (see Figure 1). Traced IRHs are marked as per the legend on panel (a). The zoomed inset on the pulse radargram shows the characteristics of R1–3 in more detail, with the color of the arrows corresponding to the legend in (a).

causing IRHs to dip significantly, or where enhanced ice-flow speeds disrupted IRH continuity, notably into the main flow features of PIG’s northern catchment. In some places, IRHs faded without such clear topography/flow-induced reasons, likely due to the attenuation of the radar signal with depth or the type of processing used (Holschuh et al., 2014). In some locations more distant from the upper PIG catchment (i.e., westward of tributary 6; Figure 1), extensive englacial layering was visible in radar profiles but, due to a dearth of connecting lines and crossovers, we could not, with confidence, identify R1–4.

When tracing between crossovers, we relied upon the distinctiveness of our IRHs. At the vertical resolution of PASIN, R1 and R2 manifest as single-amplitude peaks, with R2 representing a particularly bright reflector widely visible across our radar data (Figure 2, Figure S1). R3 consists of the shallowest of a series of closely spaced bright horizons, often manifested as a couplet (zoomed inset in Figure 2, Figure S1), and previously identified by Karlsson et al. (2014; their “Layer 2”) and Ashmore et al. (2020; their “H3”). The lowermost IRH, R4, forms the upper part of a band of bright reflectors visible at the intersection with the  $17.5 \pm 0.5$  ka layer widely imaged on radar data from the International Trans-Antarctic Scientific Expedition (ITASE) connecting the PIG catchment with the Byrd Ice Core chronology (Hammer et al., 1997; Jacobel & Welch, 2005) (Figures 1, 2, and S1).

Once R1–4 were traced through the PIG-PASIN survey, we looked for the same IRHs on the OIB-MCoRDS2 data using available crossovers between each survey (Figures 1 and 3). We found R2–3 to be equally distinguishable in OIB-MCoRDS2 profiles, with R2 representing a particularly bright reflector similar to that on PIG-PASIN, whilst R3 also formed the shallower part of an easily distinguishable couplet. We did not recover R1 independently on the OIB-MCoRDS2 profile crossing the WAIS Divide Ice Core and used intersections with PIG-PASIN to trace it across to the Institute Ice Stream catchment. Similarly, we used several intersections with the  $17.5 \pm 0.5$  ka layer from Jacobel and Welch (2005) in and around the WD2014 site to recover R4 in the OIB-MCoRDS2 data (Figures 1 and 3).

It is worth noting that the OIB-MCoRDS2 data were acquired 12–14 years later than the PIG-PASIN survey, and so the same IRHs will, in principle, lie slightly lower in the ice column. However, considering a present-day mean accumulation rate of  $\sim 0.30\text{--}0.35$  m a<sup>−1</sup> (meters of ice equivalent per year) at the intersection between the two surveys, the maximum change in IRH depth is < 5 m. This is well within the bounds of the total depth uncertainty calculated for each radar system (see Section 2.3) and does not affect the pattern

of englacial layering or the identification of our IRHs across the different surveys. Crossover analysis at key intersections on the airborne radar data showed that the mean depth difference for R1–4 falls within the uncertainty range of all surveys (Figure S2, Tables S1 and S2) (see Section 2.3). At 10 intersections on PIG-PASIN, the mean depth difference for R1–4 is  $< 6$  m. Similarly, the mean depth difference for R2–3 at 11 intersections between PIG-PASIN and OIB-MCoRDS2 is 14 and 29 m, respectively, and  $< 18$  m at 5 intersections between R4 on OIB-MCoRDS2 and the  $17.5 \pm 0.5$  ka from Jacobel and Welch (2005) (Figure S2, Table S2).

With our objective being to produce an age-depth radiostratigraphy across PIG, we converted all IRHs traced above in the time domain ( $t_{IRH}$ ) to depth ( $d_{IRH}$ ) using

$$d_{IRH} = \frac{v_{ice} t_{IRH}}{2} + Z_f, \quad (1)$$

where  $v_{ice} = 168.5 \text{ m } \mu\text{s}^{-1}$  is the speed of electromagnetic waves through ice (cf. Fujita et al., 2000) and  $Z_f = 10$  m is a spatially invariant firn correction, appropriate for West Antarctica (Ashmore et al., 2020). All our depth measurements are given in meters below the surface. We then calculated IRH depth as a function of ice thickness using the ice-thickness measurement from each respective radar mission, and complemented these with ice-thickness measurements from BedMachine (Morlighem et al., 2020) in places where the radar did not sound the bed.

### 2.3. Catchment-Wide Depth Uncertainties

To assess the accuracy of our IRH depths at the catchment scale, we consider the uncertainties associated with the imaging of IRHs with ice-penetrating-radar. These uncertainties primarily depend on three factors: variations in the speed of electromagnetic (EM) waves through the ice, the firn-density correction, and the radar system's range precision (Cavitte et al., 2016) (Text S1).

The maximum uncertainty arising from selecting an EM value ranging between 168 and  $169.5 \text{ m } \mu\text{s}^{-1}$  is 16 m on the maximum depth of the deepest reflection on PIG-PASIN and 14 m on OIB-MCoRDS2. The uncertainty associated with the firn correction is  $\pm 3$  m, owing to minor variations in firn densification across the catchment (Ashmore et al., 2020) (Text S1). The precision of IRH depth estimates also depends on the range accuracy,  $\sigma(r^*)$ , of the radar system, which refers to how accurately changes can be located in 3-D space (Cavitte et al., 2016; King, 2020). This is a combination of the SNR of each IRH and the range resolution,  $\Delta r$ , of the radar system, which is mainly a function of sampling frequency, bandwidth, source wavelets, and the type of post-processing applied. The range resolution for each system, from coarser to finer is: PASIN chirp (12.89 m), PASIN pulse (8.42 m), and MCoRDS2 (2.58 m) (Table 1, Text S1).

We undertook an empirical error analysis to calculate the maximum uncertainty associated with the deepest IRH by calculating the root-mean-square error of the depth uncertainties from EM wave through the ice, the firn correction, and the radar range accuracy. We obtained a combined maximum uncertainty of  $\pm 17$  m and attached this uncertainty to all IRHs traced on the PIG-PASIN data (Text S1). Similarly, we estimated a combined maximum uncertainty of  $\pm 14$  m on the OIB-MCoRDS2 data (Text S1). Given that this uncertainty represents the maximum uncertainty on the deepest IRH over our entire data set, we also calculate IRH-specific uncertainties at the ice-core site (see Section 2.4.1).

### 2.4. Age-Depth Attribution

To estimate the absolute age of our IRHs, we employ two primary dating methods: we use (a) the WAIS Divide ice-core chronology to provide a direct age to our three deepest IRHs, namely R2–4; and (b) the Dansgaard-Johnsen 1-D model to independently compare the ages calculated at the ice core and to provide an approximate age range to our shallowest IRH, R1. Once dated, we also compared the ages and depths of R1–3 with dated IRHs traced across PIG (Karlsson et al., 2014; Siegert & Payne, 2004) and Institute and Möller Ice Streams (Ashmore et al., 2020); as well as the age and depth of R4 with the  $17.5 \pm 0.5$  ka layer dated using the Byrd ice-core chronology (Hammer et al., 1997) and traced across the WAIS (Jacobel &

Welch, 2005). Finally, we also compare the depth and age of our upper three IRHs with sulfate concentrations from the WD2014 ice-core record (Cole-Dai, 2014; McConnell et al., 2017).

### 2.4.1. Connection to the WAIS Divide Ice-Core Chronology

We used the 2016 OIB-MCoRDS2 data linking central PIG to the WD2014 site to date IRHs across PIG relative to the ice-core chronology, where annual-layer counting goes back to the last ~31 ka BP (Buizert et al., 2015; Sigl et al., 2016). We take the recorded depth at the ice core which most-closely matches our IRH depth at WD2014, and calculate the upper and lower age bounds using the radar depth and ice-core

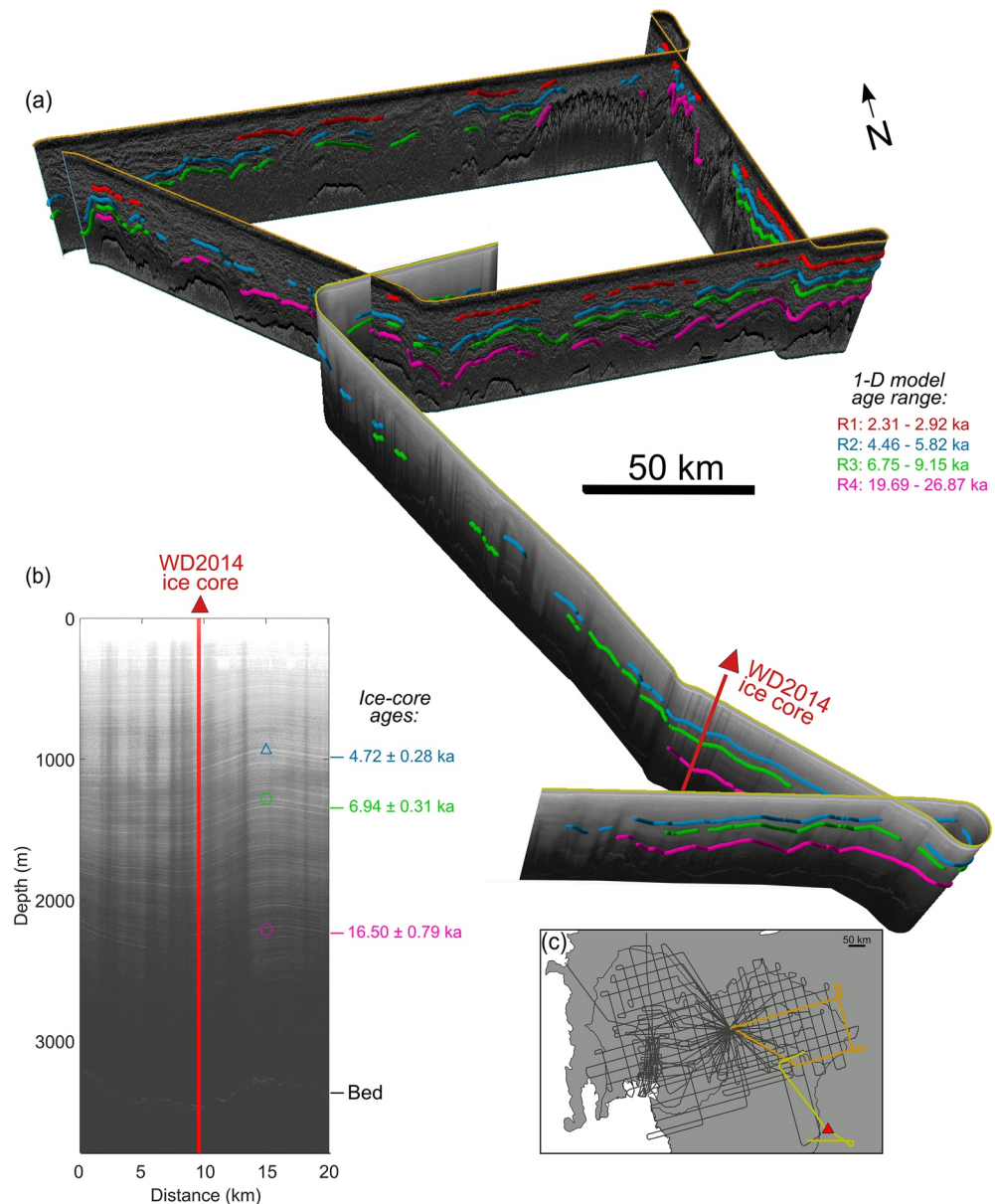


**Figure 3.** (a) Intersecting radar profiles from PIG-PASIN and OIB-MCoRDS2 with IRHs R1 (red), R2 (blue), R3 (green), and R4 (pink) traced along radargrams. The age range shown on the PIG-PASIN profile in the top right corner is from the 1-D model for R1–4 (see Section 3.2). (b) Englacial layering on the OIB-MCoRDS2 radar profile where it intersects the WD2014 ice core (red line), with ages and total age uncertainties for R2–4 inferred from the ice-core chronology (see Section 3.2) shown on the right-hand side. (c) Inset showing the PIG-PASIN (orange line) and OIB-MCoRDS2 (yellow line) profiles in (a) and the full PIG-PASIN radar flight lines shown in gray in the background, as well as the position of the WD2014 ice core (red triangle).

uncertainties. Following MacGregor et al. (2015), the age uncertainty ( $\Delta a_{comb}$ ) associated with each IRH is the root-mean-square combination of the age uncertainty associated with the unweighted mean IRH depth at the ice core ( $\Delta a_{\Delta depth}$ ) and the age uncertainty associated with the ice core at the IRH depth ( $\Delta a_{core}$ ), following

$$\Delta a_{comb} = \sqrt{\Delta a_{\Delta depth}^2 + \Delta a_{core}^2}, \quad (2)$$

where ( $\Delta a_{core}$ ) is a function of the age of the individual IRH at the ice core site (Sigl et al., 2016) and the published uncertainty associated with the ice core age (1% and 3% for ages ranging between 0–15 ka and 15–31 ka BP, respectively; Sigl et al., 2016), while ( $\Delta a_{\Delta depth}$ ) is a function of the depth uncertainty of each IRH at the ice-core site. Since the uncertainty in the EM wave through the ice increases with depth, using the maximum uncertainty calculated on the deepest IRH to calculate  $\Delta depth$  at a catchment scale (see Section 2.3) would result in less accurate age uncertainties at the ice core. We have therefore calculated a depth uncertainty for each individual IRH at the ice core, and undertook the same empirical error analysis to calculate  $\Delta depth$  at WD2014. This resulted in IRH-specific radar depth uncertainties which we used to calculate the age uncertainty for each IRH at WD2014, as per Equation 2.

Whilst  $\Delta a_{comb}$  represents the combined maximum uncertainty from the radar and the ice-core chronology, we found that our IRHs are systematically lower in the ice column compared with strong peaks in acidity concentrations at WD2014 matching closely the age and depth of our IRHs and which we can assume to be the likely cause of our IRHs (see Section 4.2). To account for this offset in ages between the IRHs and the strong sulfate peaks observed at WD2014, we calculated a total age uncertainty ( $\Delta a_{total}$ , Table 3) which represents the maximum age difference between our IRHs and the sulfate peaks at the ice core. This was obtained by adding a systematic factor of 0.22 ka to  $\Delta a_{comb}$ , which represents the total age difference between the maximum IRH age calculated using  $\Delta a_{comb}$  and the age of the strong sulfate peaks (see Section 4.2). We provide the total uncertainty values in Table 3 and Section 3.2.

#### 2.4.2. Age-Depth Modeling

To provide an independent validation of our ice-core derived IRH ages, we also applied the Dansgaard and Johnsen (1969) 1-D vertical ice-strain rate model to derive approximate dating of the IRHs traced over the central PIG catchment. This model has been used previously to date IRHs across West Antarctica (Ashmore et al., 2020; Corr & Vaughan, 2008; Karlsson et al., 2012, 2014), assess divide migration (Waddington et al., 2005), and calculate past accumulation rates at or near ice divides (Jacobel & Welch, 2005; Siegert & Payne, 2004). We chose the Dansgaard-Johnsen model here for its simplicity and as it allows us to test the effect of ice deformation on the ages of our IRHs. However, we note that other alternatives exist such as the Nye (1957) and Lliboutry (1979) models, or the more developed quasi-Nye model (MacGregor et al., 2015).

Under the assumption that the ice sheet is, and has been, in steady state, close to an ice divide, the Dansgaard-Johnsen model gives

$$t = \frac{2H - h}{2a} \ln \left( \frac{2H - h}{2z - h} \right), h \leq z \leq H, \quad (3)$$

where  $t$  (ka; thousand years) is the age of an IRH,  $H$  (m) is the ice thickness (assumed constant in time),  $h$  (m) is the thickness of the basal shear layer,  $a$  (in  $\text{m a}^{-1}$  ice-equivalent) is the average accumulation rate since deposition of the IRH, and  $z$  (m) is the elevation of the IRH above the bed (Dansgaard & Johnsen, 1969).

For this model, several assumptions are made: (a) negligible horizontal velocity component; (b) time-averaged accumulation rates and no temporal change in accumulation patterns; and (c) constant ice deformation from the surface to some depth,  $h$ , below which vertical strain rate is assumed to decrease linearly toward the bed. Considering the above, we initiated the model on the PIG-PASIN data at two sites (A and B in Figure 1) located  $\sim 50$  km from the ice divide where horizontal ice flow is minimal ( $< 3 \text{ m a}^{-1}$ ), the ice



is thick (>3 km) and the bed relatively flat. Site A (80.15°S, 101.56°W) was selected due to its relative proximity within PIG to WD2014 (~215 km). At this site, R1–3 were traced, as well as R4. This provided us with initial constraints for age-depth estimates for the upper IRHs (namely R1–3), and allowed us to evaluate the model results based on the approximate known age of R4. To ensure representativeness, however, we also selected a second site, Site B (79.87°S, 100.03°W), where R1–3 were traced but not R4.

We based our estimates for  $a$  in the equation on advection-corrected accumulation rates from the WD2014 ice core (Fudge et al., 2016) for each IRH R1–4, and with current accumulation estimates to correct for any elevation-dependent change in accumulation between the WD2014 site and our PIG Sites A and B. Tentatively treating our R1–3 as broadly equivalent to three of Siegert and Payne's (2004) dated IRHs based on depth associations at three crossovers (see Text S2, Table S3), we derived mean advection-corrected accumulation rates at WD2014 for each reference age:  $0.247 \pm 0.062 \text{ m a}^{-1}$  (3 ka BP, with BP defined as years before 1950 CE),  $0.248 \pm 0.062 \text{ m a}^{-1}$  (5 ka BP), and  $0.243 \pm 0.061 \text{ m a}^{-1}$  (7 ka BP), as well as a rate of  $0.226 \pm 0.051 \text{ m a}^{-1}$  (17.5 ka BP) based on the intersection with Jacobel and Welch (2005). The errors correspond to uncertainties in the firn-densification model used by Fudge et al. (2016). These provide us with estimates of what would be required to reproduce each layer if accumulation had remained constant between the time of the deposition of the layer and the present at WD2014. Under the assumption that spatial accumulation patterns have not changed during the Holocene over the WAIS (Koutnik et al., 2016; Neumann et al., 2008; Siegert & Payne, 2004), and considering that accumulation rates at the Ice Core are generally smaller than at Sites A and B (Table S4), we use modern accumulation rates from modeled and observational data to calculate the regional difference between accumulation at WD2014 and our Sites A and B. The four sources of accumulation data used here are: (a) SMB estimates for the period 1979–2015 using the Modèle Atmosphérique Régional (MAR, Version 3.6.4; Agosta et al., 2019); (b) SMB estimates for the period 1979–2018 from the Regional Atmospheric Climate Model 2 (RACMO2; van Wessem et al., 2018); (c) accumulation rates interpolated from ground measurements and AMSR-E polarisation (Arthern et al., 2006; hereafter referred to as ART06); and (d) a combination of catchment-wide, snow and accumulation radar measurements obtained in 2009–11 from ultra-wideband airborne platforms and intersecting a series of shallow ice cores (Medley et al., 2014), combined with a set of GPR tracks acquired in 2002–04 over the Western Divide (Neumann et al., 2008) (hereafter referred to as MED14) (Text S2). From these data sets, we calculate a percentage of change between WD2014 and Sites A and B and apply this to the mean advection-corrected rates calculated at WAIS Divide for R1–4 (Table S4). Together, these provided us with a range of realistic values of  $a$  for each IRH at Sites A and B to use as input into the 1-D model.

The thickness of the basal shear layer,  $h$ , is largely unknown as it is dependent on accurate knowledge of the bed topography and temperature of the ice (Neumann et al., 2008). Previous studies have used a value of  $h = 400 \text{ m}$  for Greenland and West Antarctica (Fahnestock et al., 2001; Jacobel & Welch, 2005; Karlsson et al., 2012; Siegert & Payne, 2004), whilst Karlsson et al. (2014) and Ashmore et al. (2020) explored the effects of fuller ranges of  $100 \text{ m} \leq h \leq 1200 \text{ m}$ . We refined this range to  $0.2H \leq h \leq 0.3H$  (Neumann et al., 2008), rounding to the nearest 100, hence investigating the effect of  $h$  ranging from 700 to 1,100 m at both sites (Text S2). We note, however, that large uncertainties in basal deformation at WD2014 (Cuffey et al., 2016; Fudge et al., 2019) could result in  $h$  values being smaller than 20% of the ice thickness and thus lead to an overestimation of our ages (see Text S2).

### 3. Results

#### 3.1. Englacial Stratigraphy

We successfully traced four IRHs R1–4 across a large proportion of the PIG catchment, including in areas where annual velocities reach up to  $\sim 350 \text{ m a}^{-1}$  (Figure 4). The most extensive IRH traced in our study is R2, closely followed by R3 (Figure 4), with mean depths across the catchment of 1,175 and 1,463 m, respectively (Table 2). The shallowest IRH, R1, was located on average at  $\sim 30\%$  of the ice depth, whilst the deepest, R4, was on average found at  $\sim 68\%$  depth (Table 2).

The traceability of R1–3 does not vary greatly and is primarily constrained by topography (Figures 4a–4c). By contrast, R4 was only detected across the upper Thwaites/PIG catchments (Figure 4d), even though

**Table 2**  
Summary Statistics for Each IRH Traced Throughout the PIG-PASIN and OIB-MCoRDS2 Surveys

	IRH depth statistics							
	Depth below the surface (m)				Depth as fraction of ice thickness			
	Mean	1 $\sigma$	Range	IQ range	Mean	1 $\sigma$	Range	IQ range
R1	722	191	204–1,302	623–873	0.30	0.10	0.12–0.63	0.22–0.36
R2	1,175	240	304–2,014	1,069–1,347	0.46	0.09	0.21–0.82	0.40–0.52
R3	1,463	298	650–2,486	1,324–1,650	0.54	0.08	0.29–0.82	0.48–0.60
R4	1,929	257	697–2,640	1,799–2,080	0.68	0.05	0.42–0.92	0.66–0.71

Note. We provide these for both depths below the surface and depth as a fraction of ice thickness. “1 $\sigma$ ” refers to one standard deviation, “Range” refers to the minimum and maximum values, and “IQ range” refers to the interquartile range (25th and 75th percentile). A maximum uncertainty of  $\pm 17$  m is assumed here.

it has previously been detected much further north into the PIG basin in the ITASE survey (Jacobel & Welch, 2005), likely due to the different frequency range used by the two radar systems. We come back to this point in Section 4.1. We were also able to trace R1–3 in the upper parts of the Institute and Möller ice-stream catchment, and R2–4 in the upper parts of the Thwaites catchment toward the WD2014 site (Figure 4). The traced IRHs are generally deeper southward of the onset of PIG tributaries 7 and 9 and at the center of the PIG catchment, and relatively shallow at its southern margin and at the divides with Thwaites Glacier and Institute Ice Stream (Figures 4e–4h). We were unable to identify the IRHs in several locations, mainly north of the main trunk of PIG near the Hudson Mountains range and west of tributary 6 (Figure 4a). We were also unable to detect continuous IRHs in any PIG-PASIN profiles traversing the main trunk and tributaries of Thwaites Glacier, nor those that cover the main trunk and fast-flowing tributaries of PIG (Figure 4).

### 3.2. Age-Depth Estimates

Having clearly identified R2–4 near the WD2014 site, we attempt to date these using the WD2014 chronology. The OIB-MCoRDS2 radar profile passes within  $\sim 1.2$  km of the ice-core site, and the stable ice conditions in the area mean that flow-induced disturbance on layer geometry is relatively limited (Laird et al., 2010). Following MacGregor et al. (2015), we calculate the unweighted mean reflection depth within a distance of  $\pm 250$  m along transect from the trace that is closest to the ice-core site to obtain  $\Delta a_{\Delta depth}$ , resulting in mean depths at the ice core of  $1,060 \pm 7$  (R2),  $1,430 \pm 9$  (R3), and  $2,371 \pm 14$  m (R4) (Table 3). Considering the radar-depth and ice-core uncertainties (Equation 2), and to account for the age offset between our IRHs and

the strong sulfate peaks at the ice core (see Sections 2.4.1 and 4.2), we determined the age and associated age uncertainty for each IRH at WD2014 as:  $4.72 \pm 0.28$  (R2),  $6.94 \pm 0.31$  (R3), and  $16.50 \pm 0.79$  ka (R4) (Table 3).

To compare the ages independently from the WD2014 chronology and provide an approximate age-range estimate for our shallowest isochrone R1, we use the 1-D model at Sites A and B. The age estimates returned from the 1-D model at both sites are as follows: R1 (2.31–2.92), R2 (4.46–5.82), R3 (6.75–9.15), and R4 (19.69–26.87 ka) (Table 4).

The ages calculated for R2–3 at WD2014 (Table 3) are within the upper and lower bounds of the modeled age-range estimates from the 1-D model (Table 4), with the MED14 and RACMO2 accumulation products best able to reproduce the ages at WD2014 to within  $< 10\%$ . However, the returned age estimate for R4 at Site A,  $19.69$ – $26.87$  ka, is  $20\%$ – $60\%$  greater than the age of R4 at WD2014 ( $16.50 \pm 0.79$  ka) and that of Jacobel and Welch (2005) ( $17.5 \pm 0.5$  ka). We come back to these points in Sections 4.1 and 4.3.

**Table 3**  
IRH Mean Depths (m), Ages (ka; in Years Before 2020 AD), and Uncertainties ( $\Delta$ ) at the WD2014 Site for R2–4

	Depth (m)	$\Delta depth$ ( $\pm m$ )	a (ka)	$\Delta a_{\Delta depth}$ ( $\pm ka$ )	$\Delta a_{core}$ ( $\pm ka$ )	$\Delta a_{comb}$ ( $\pm ka$ )	$\Delta a_{total}$ ( $\pm ka$ )
R2	1,060	7	4.72	0.04	0.05	0.06	0.28
R3	1,430	9	6.94	0.06	0.07	0.09	0.31
R4	2,371	14	16.50	0.28	0.50	0.57	0.79

Note. Column “a (ka)” refers to the IRH age obtained from the radar-depth and the depth at the WD2014 ice core. Column “ $\Delta a_{comb}$ ” refers to the combined age uncertainty from the radar and the ice-core chronology, whilst “ $\Delta a_{total}$ ” refers to the maximum age uncertainty of our IRHs calculated from the age difference between our IRHs and the strong sulfate peaks at WD2014 (see Sections 2.4.1 and 4.2).

Abbreviation: IRH, internal reflecting horizon.

**Table 4**  
Modeled IRH Age-Range Estimates (ka) Returned From the 1-D Steady-State Model for Varying Accumulation Data Sets (see Section 2.4.2) and Basal Shear Layer Thickness ( $h$ , in m) Scenarios at Sites A and B for IRHs R1–4 (see Section 2.4.2)

		Site A			Site B		
		$h = 700$	$h = 900$	$h = 1,100$	$h = 700$	$h = 900$	$h = 1,100$
R1	MAR	2.84	2.85	2.86	2.89	2.90	2.92
	ART06	2.68	2.69	2.70	2.78	2.80	2.81
	RACMO2	2.36	2.37	2.38	2.32	2.33	2.34
	MED14	2.31	2.32	2.33	2.36	2.37	2.38
R2	MAR	5.72	5.77	5.82	5.55	5.61	5.67
	ART06	5.40	5.44	5.49	5.35	5.40	5.46
	RACMO2	4.75	4.79	4.84	4.46	4.50	4.55
	MED14	4.65	4.69	4.73	4.57	4.62	4.67
R3	MAR	8.88	9.01	9.15	8.41	8.54	8.69
	ART06	8.38	8.50	8.63	8.10	8.23	8.37
	RACMO2	7.38	7.48	7.60	6.75	6.86	6.98
	MED14	7.22	7.32	7.43	6.92	7.03	7.15
R4	MAR	24.22	25.40	26.87	–	–	–
	ART06	22.85	24.00	25.40	–	–	–
	RACMO2	20.13	21.10	22.32	–	–	–
	MED14	19.69	20.64	21.84	–	–	–

Note: At Site B, R4 was not retrieved. The accumulation rates ( $\text{m a}^{-1}$ ) used to obtain each IRH age estimate can be found in Table S4. We calculate an empirical error estimate of between  $\pm 2\%$  and  $4\%$  for each modeled age estimate based on the uncertainties in radar depth ( $\pm 17$  m) and ice thickness ( $\pm 23$  m, Vaughan et al., 2006).

Abbreviation: IRH, internal reflecting horizon

## 4. Discussion

### 4.1. IRH Comparison Across the WAIS

Karlsson et al. (2014) traced two distinctive IRHs through the middle ice depths across parts of the central PIG catchment using the same PIG-PASIN data set as that used here, but only focusing on flight lines flown at constant elevation and only exploiting the data in its chirp mode. This earlier study highlighted the existence of a distinctive IRH package between an upper bound, “Layer 1”, approximately dated to 5.3–6.2 ka, and a lower bound “Layer 2”, approximately dated to 8.6–13.4 ka. Here, by additionally exploiting the full spatial extent of the PIG-PASIN data set, the simultaneously acquired pulse-mode PASIN data, and complementing these with recent OIB-MCoRDS2 data, we have expanded the reach of that earlier radiostratigraphy across the fuller PIG catchment, and across the ice divides into neighboring regions, notably Thwaites Glacier and Institute Ice Stream. Direct comparison between both sets of results suggests that Karlsson et al.’s (2014) Layers 1 and 2 are equivalent to the IRHs traced in this study as R2 and R3, with a median difference ranging between 6 and 12 m, which is within the depth uncertainty of the IRHs (Figure S3).

Throughout the neighboring Institute and Möller ice-stream catchments, Ashmore et al. (2020) also recently traced three prominent IRHs (H1–3), broadly dated at 1.9–3.2 (H1), 3.5–6.0 (H2), and 4.6–8.1 ka (H3), using the same 1-D model described here. They posited that their deeper two IRHs (namely H2–3) were also similar to Karlsson et al.’s (2014) Layers 1 and 2 (and hence are likely equivalent to our R2 and R3), but the association was untested with any direct crossovers. Here, we were able to trace our upper three IRHs R1–3 along an OIB-MCoRDS2 profile extending across the upper Institute Ice Stream catchment (Figures 4a–4c), intersecting eight IMAFI-PASIN profiles in which H1–3 were traced. Across these intersections, the mean difference between OIB-MCoRDS2 R1–3 and IMAFI-PASIN H1–3 is 15 m, which is within the uncertainty bounds of the respective radar systems ( $\pm 14$  m for OIB-MCoRDS2;  $\pm 15$  m for IMAFI-PASIN, Ashmore

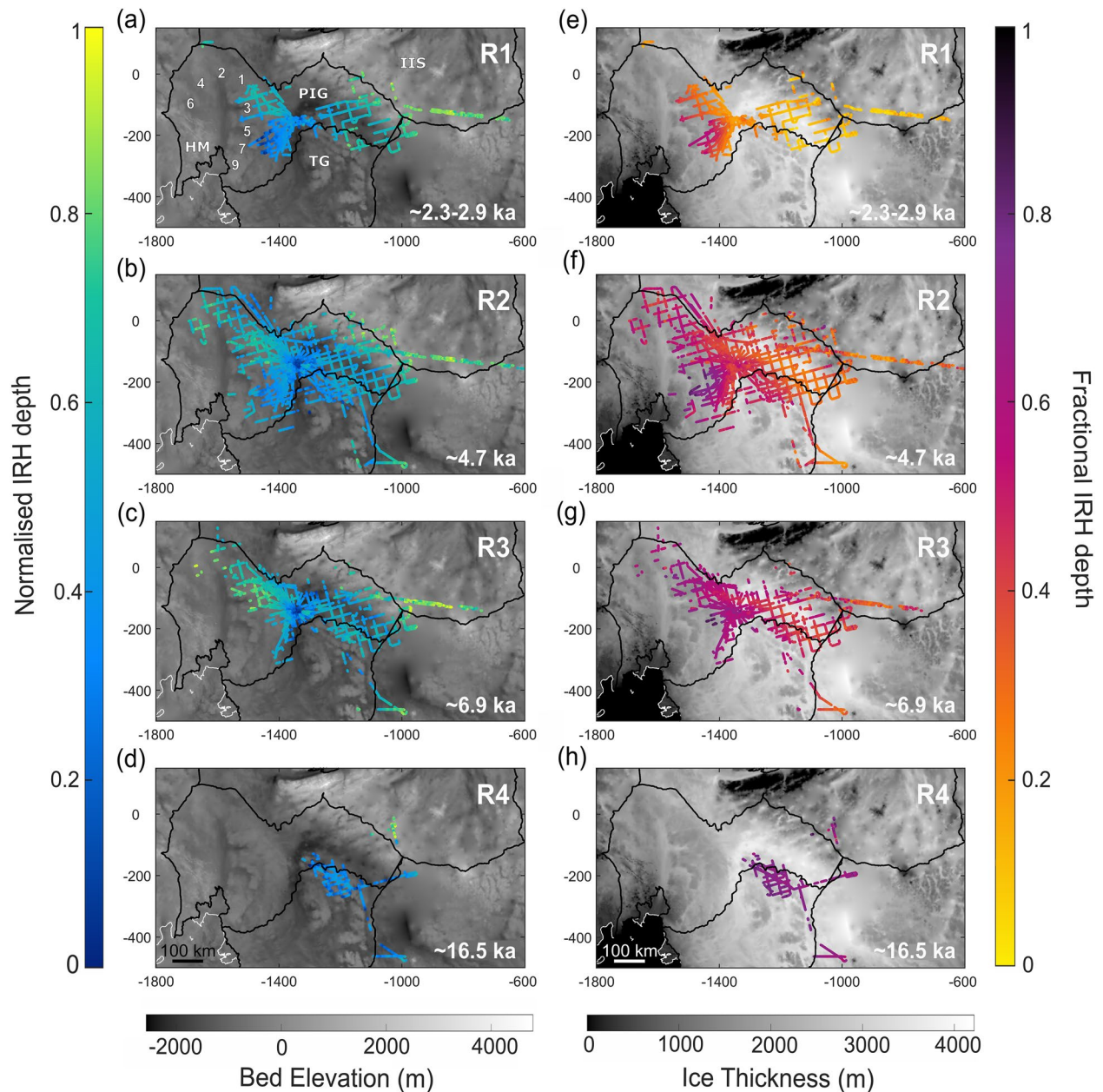


**Figure 4.** Normalized (a–d) and fractional (e–h) depth for the four IRHs traced over the PIG-PASIN and OIB-MCoRDS2 data from shallowest to deepest. Also shown are the IRH ages (ka) (see Section 3.2) for R1 (age-range estimate from 1-D model) and R2–4 (ages from WD2014 ice-core intersection). For (a–d), lower (blue) values correspond to relatively deep IRH depths, higher (yellow) values correspond to shallow IRH depths. Background is bed elevation in meters (referenced to the WGS84 ellipsoid) from BedMachine (Morlighem et al., 2020). For (e–h), lower (yellow) values correspond to the shallowest IRHs, higher (purple) values correspond to the deepest IRHs. Background is ice thickness in meters from BedMachine (Morlighem et al., 2020). The white line is the Antarctic coast line. The numbers and annotations in (a) are the eight fast-flowing tributaries (1–7 and 9) of Pine Island Glacier, the location of the Hudson Mountain Range (HM), and the ICESat IMBIE basins containing Pine Island Glacier (PIG), Thwaites Glacier (TG) and Institute Ice Stream (ISS) (Zwally et al., 2012).

et al. 2020), and hence provides additional evidence that we observe the same IRHs across both catchments. Two sets of parallel profiles, laterally offset by ~1.5 km, and acquired across the PIG/Institute Ice Stream divide in the PIG-PASIN and IMAFI-PASIN data sets (Figure 1), provide a further opportunity to confirm these equivalences with data from the same radar system. Only in three short sections of these transects could we compare our IRHs with those from the IMAFI-PASIN study (inset Figure S3a); in these locations,

we could not identify R1 and R3. Nevertheless, at two intersections (black arrows in inset on Figure S3a), the respective depths for PIG-PASIN R2 and IMAFI-PASIN H2 were 794 and 797 m at Intersection 1 and 776 and 778 m at Intersection 2, respectively, which is remarkably close considering ice thickness in this area exceeds 2 km. This, alongside the crossovers on the OIB-MCoRDS2 data, gives us high confidence that our R2, Ashmore et al.'s (2020) H2, and therefore Karlsson et al.'s (2014) Layer 1, all represent the same internal marker in the ice. This study, by using additional data that allowed direct dating at the WD2014 site, is therefore able to ascribe more accurate and precise ages to the IRH package ranging across PIG and Institute and Möller Ice Streams of  $4.72 \pm 0.28$  ka (Layer 1/H2/R2) and  $6.94 \pm 0.31$  ka (Layer 2/H3/R3), respectively, based on the WD2014 ice-core chronology.

We also note that all three studies identify R2 as their most spatially extensive IRH, indicating the presence of a particularly ubiquitous isochrone, similar in age to a  $4.72 \pm 0.24$  ka isochrone detected and also extensively mapped elsewhere across central West Antarctica (Muldoon et al., 2018). Whilst we were not able to provide a more refined age to our shallowest IRH, R1, from direct intersection of the WD2014 Ice Core, the 1-D model returned an age-range estimate (2.31–2.92 ka) that is in broad agreement with that of Ashmore et al. (2020) (1.9–3.2 ka; their H1) and Siegert and Payne (2004) ( $3.10 \pm 0.16$  ka; their L07). Together, these studies demonstrate considerable promise for unifying an age-depth stratigraphy across the WAIS back to at least  $\sim 7$  ka, while tying our IRHs to the WD2014 Ice Core has yielded more accurate, and younger, ages, for the isochrones detected across PIG and, by extension, Institute and Möller Ice Streams.

The age assigned to R4 at WD2014 ( $16.50 \pm 0.79$  ka) is slightly younger than the  $17.5 \pm 0.5$  ka layer tied by Jacobel and Welch (2005) to the Byrd Ice Core (Hammer et al., 1997), although there is an overlap of 0.29 ka when fully accounting for the age uncertainties. We offer two potential explanations for this disparity. First, the low-frequency ground-radar system used as part of the ITASE survey has a much longer wavelength than the high-frequency airborne systems used here, meaning that the  $17.5 \pm 0.5$  ka layer appears as a single-amplitude peak measuring tens of meters in thickness (cf. Jacobel & Welch, 2005), whereas the shorter-wavelength on the airborne radars allows for the delineation of individual peaks, thus resolving the strong singular reflector from Jacobel and Welch (2005) as a series of closely spaced reflectors. As a result, when attempting to connect the ITASE profile with the airborne radar data, it is likely that the closest bright reflector identified on the airborne radar forms the upper part of the wider reflector imaged by Jacobel and Welch (2005), thus leading to younger ages at the intersection with the WD2014 Ice Core. Second, the uncertainties in the radar data at the intersection between OIB-MCoRDS2 ( $\pm 14$  m) and Jacobel and Welch's (2005) profile ( $\pm 10$  m) increase the chance to misinterpret the correct position of the 17.5 ka layer over the airborne data, although we show in Table S2 that the mean depth difference between R4 and Jacobel and Welch's (2005) layer is  $< 18$  m, which is within the uncertainty range of both studies. Whilst these points are relevant when comparing the ages of R4 at WD2014 with the age of Jacobel and Welch's (2005) layer, it is worth mentioning that the exact age and depth of the strong reflector at WD2014 are known from electrical conductivity and chemistry measurements. At the ice core, this layer is characterized by nine distinctive peaks ranging in depths between 2,420 and 2,427 m and dated at  $17.75 \pm 0.19$  ka (McConnell et al., 2017; Sigl et al., 2016), a full 35 m below the depth of R4 at WD2014. Even taking into account the maximum depth of our IRH along the  $\pm 250$  m transect ( $2,378 \pm 14$  m; see Section 3.1), R4 is still found 28 m above the depth of the  $17.75 \pm 0.19$  ka at WD2014. Considering all the above, it is likely that R4 is not the same layer as the strong volcanic layer dated at  $17.75 \pm 0.19$  ka at WD2014 (McConnell et al., 2017), but rather forms the upper part of the wide reflector imaged by Jacobel and Welch (2005) in the ground-radar data.

#### 4.2. Linkage with the WAIS Divide Ice-Core Record

Whilst determining the cause of R4 remains ambiguous due to the limitations mentioned above, the existence of R2 and R3 offers an opportunity to link them directly to the ice-core sulfate record at WD2014. High sulfate content from volcanic sulfuric acid is known to correspond to high acidity levels in englacial layers in ice cores (Castellano et al., 2005; Gow & Williamson, 1971; Hammer et al., 1997; Millar, 1982) and, because the radar is sensitive to acidity contrasts (Fujita et al., 1999; Millar, 1981), we can attempt to link the sulfate record at the ice core with our IRH stratigraphy. Figure S4 shows the presence of three large peaks in sulfate concentration at the WD2014 ice core, which are particularly close in age and depth to IRHs R2–3 traced on the OIB-MCoRDS2 profile near WD2014. In particular, a layer dated at 4.94 ka (depth: 1,099 m)

contains sulfate concentrations that are unmatched ( $405 \mu\text{g}/\text{kg}$ ) for much of the core up until a depth of  $\sim 2,400$  m (equal to the last  $\sim 18,000$  years BP) (Figure S4). Even taking into account the entire profile, this layer contains the fourth largest amount of sulfate concentrations in the last  $\sim 68,000$  years BP. We also notice the presence of two closely spaced peaks in the sulfate record which are dated at 7.25 ka (depth: 1,475 m; sulfate concentration:  $306 \mu\text{g}/\text{kg}$ ) and 7.64 ka (depth: 1,526 m; sulfate concentration:  $271 \mu\text{g}/\text{kg}$ ), corresponding to the 9th and 10th highest sulfate concentrations on record (Figure S4b). Not only do these ages match closely the age of R3 at the ice core, they also match the characteristics of R3, which is often found as a couplet across most of Pine Island, upper Thwaites, and Institute and Möller ice-stream catchments on the airborne radar data (Figures 2 and S1). Additionally, the second largest peak on record before  $\sim 18,000$  years BP is found at a depth of 584 m and dated at 2.45 ka (sulfate concentration:  $309 \mu\text{g}/\text{kg}$ ), which falls within the modeled age-range estimate for R1 (2.31–2.92 ka) at Sites A and B (Table 4, Figure S4a).

Whilst this offers us the opportunity to directly link our IRHs to the WAIS Divide record, we note that the depths of R2–3 at WD2014 are slightly shallower (R2:  $1,060 \pm 7$  m; R3:  $1,430 \pm 9$  m) than the sulfate peaks in Figure S4, resulting in slightly younger ages at the ice core. We cannot exclude the possibility that we traced a layer that is slightly above R2 and R3 at the Ice Core, although this is unlikely as we base our tracing on depth intersections (Figure S2) and IRH characteristics (Figure S1). Even taking into account the maximum depth of R2–3 along our  $\pm 250$  m transect to account for the fact the OIB-MCoRDS2 line did not fly directly over the WD2014 site but instead  $\sim 1.2$  km away (see Section 2.4.1), R2 ( $1,069 \pm 7$  m) and R3 ( $1,438 \pm 9$  m) would still be found 23 and 28 m higher than the sulfate peaks at the ice core, respectively. Whilst this is a relatively small disparity considering ice thickness in the area exceeds  $\sim 3.5$  km and that we are effectively comparing airborne-radar data (meter-scale accuracy) with ice-core data (mm-scale accuracy), the reason for our IRHs not aligning more closely with the sulfate peaks remains unclear. One potential explanation could relate to the distance between our transect and the location of the WD2014 ice-core site. Although Laird et al. (2010) suggested that flow-induced disturbance on layer geometry is limited in the area around the WD2014 site, changes in bed roughness were found to affect englacial stratigraphy near WD2014. This could lead to small undulation in IRH elevations between our transect and WD2014 and thus cause in several meters of discrepancy. To acknowledge this, and considering that the sulfate peaks are most likely the cause of our IRHs as we show above, we have increased the age uncertainty of our IRHs to account for the offset between our IRH ages and the age of the sulfate peaks (see Section 2.4.1, Table 3). This results in more conservative uncertainties for our deeper three IRHs dated at the ice core:  $4.72 \pm 0.28$  (R2),  $6.94 \pm 0.31$  (R3), and  $16.50 \pm 0.79$  ka (R4).

By linking three of our four IRHs to the sulfate record at WAIS Divide, we can hypothesize that the origin of our spatially extensive IRHs is from past explosive volcanic activity during the Holocene. Previous studies in Antarctica have demonstrated the correspondence between bright reflectors in radar data and past volcanic activity (e.g., Corr & Vaughan, 2008; Jacobel & Welch, 2005). Karlsson et al. (2014) previously attempted to link their deeper layer (Layer 2/R3) to acidity peaks at Byrd Ice Core; however, the absence of a direct link between the PIG catchment and a complete ice-core chronology was lacking at the time. The evidence presented here suggests that our IRHs may also originate from past explosive volcanism; but, the precise source of these eruptions, whether regional or global, remains unknown.

#### 4.3. Accumulation Rate and IRH-Age Comparison

The correspondence in isochrone-age estimates for IRHs R2–3 derived from intersecting the WD2014 site (Table 3) and using the 1-D model (Table 4) at the PIG/Thwaites divide ( $\sim 250$  km away) (our Sites A and B; Figure 1) suggests that accumulation patterns have remained broadly similar across the Amundsen-Ross divide for at least the last  $\sim 7$  ka. Whilst this is based on a relatively limited amount of data points, it complements previous studies (Fudge et al., 2016; Koutnik et al., 2016; Neumann et al., 2008), including Siegert and Payne (2004) who, using the same SPRI/NSF/TUD radar transect as that in Figure 1, concluded that accumulation patterns have remained stable over the last 6.4 ka. We suggest future research make use of the accurately dated IRHs provided here to model Holocene accumulation rates and patterns, as well as regional ice-sheet balance velocities, as previously conducted over Greenland (e.g., MacGregor et al., 2016)

and on individual sections of the WAIS (Koutnik et al., 2016; Neuman et al., 2008). This will provide additional information on the terrestrial ice-sheet history of the ASE during the Holocene, and in turn help us to constrain better the future of the WAIS.

Previous studies have successfully combined ice-core records with modeled modern-day accumulation rates to reconstruct Holocene accumulation (Cavitte et al., 2018; Fudge et al., 2016; Nielsen et al., 2018), although non-climatic noise in the observations and model biases have resulted in small discrepancies between ice-core and model reconstructions (Cavitte et al., 2020; Dalaiden et al., 2020). When assessing the ability of the 1-D model to reproduce the ages for R2-3 derived at the WD2014 Ice Core, we find that the best match (to within < 10%) is achieved using the modern accumulation rates provided by the MED14 and RACMO2 products. This is not surprising as both have higher spatial resolution than MAR and ART06, but it also likely reflects the fact that MED14 is an observational product and that RACMO2 has been shown to agree well with geophysical estimates of accumulation rates (Lenaerts et al., 2012; Medley et al., 2014; van Wessem et al., 2018; Wang et al., 2016). In contrast, when using present-day accumulation estimates from ART06 and MAR to calculate past accumulation rates, model-derived ages are up to 1.1 ka (~23%) greater for R2 and 2.2 ka (~32%) greater for R3 compared with ice-core derived ages (Tables 3 and 4). This discrepancy is primarily dominated by different modern accumulation gradients estimated between WD2014 and the PIG/Thwaites divide (i.e., Sites A and B), with the MED14 and RACMO2 products suggesting a slightly more homogenous gradient than ART06 and MAR (Table S4). Lower in the ice, the poor correspondence between the age of R4 derived by links to the WD2014 ( $16.50 \pm 0.79$  ka) relative to the age returned by the 1-D model (19.69–26.87 ka) is worthy of investigation. Even taking into account the maximum age uncertainty at the ice core, the minimum and maximum age returned by the 1-D model is 2.6 (15%) and 9.8 ka (57%) greater than at the ice core (Tables 3 and 4), a difference that cannot solely be attributed to the different modern-day accumulation gradients mentioned above. The most likely explanation is that the assumptions required for the 1-D model (see Section 2.4.2) break down for older IRHs, where local accumulation rate is no longer a primary factor in determining the depth of an IRH. This could be due to complex flow dynamics such as longitudinal strain or lateral shearing at the boundary between slow and fast-flowing ice, resulting in high internal stress impacting IRH stratigraphy in the deeper part of the ice column (Waddington et al., 2007). Moreover, R4 ( $16.50 \pm 0.79$  ka) was deposited pre-Holocene as the WAIS was transitioning from a glacial to an interglacial period during which ice thickness has likely not remained constant (Golledge et al., 2014; Johnson et al., 2017), implying possible changes in ice-flow configurations for which the steady-state model is not able to account.

#### 4.4. Characteristics of Englacial Stratigraphy

Previous research over East Antarctica has shown that common bright reflectors can be interchangeably traced over long distances using radar systems operating at different center frequencies (Cavitte et al., 2016; Winter et al., 2017). Our findings provide further evidence of this over West Antarctica, having successfully identified common IRHs across different airborne radar systems. However, although IRHs younger than 7 ka can be traced widely across the WAIS using existing data sets, tracing deeper, pre-Holocene IRHs has not been widely possible across PIG (this study) nor the Weddell Sea Sector (Ashmore et al., 2020). Relative to the interior of East Antarctica, where much lower snow accumulation and ice-flow velocities have facilitated the tracing of isochrones pre-dating the LGM (~20 ka BP) and even the past glacial-interglacial periods (up to ~366 ka BP) (Cavitte et al., 2016; Parrenin et al., 2017; Steinhage et al., 2013; Winter et al., 2019), the extremely variable deep-ice conditions in the WAIS will challenge the recovery of pre-Holocene radiostratigraphy. Compounding the challenge, Ross et al. (2020) have demonstrated that large packages of ice older than ~16 ka in the Weddell Sea sector of the WAIS are rheologically different to the ice above, containing large proportions of deformed and folded ice. These packages typically show poor continuity of englacial stratigraphy across Institute and Möller Ice Streams (Bingham et al., 2015) and, indeed, where we could see IRHs deeper than R4 in PASIN and MCoRDS2 for this study, very few were continuous for long distances. Over other parts of the WAIS, an IRH dating back to  $24.9 \pm 0.3$  ka has been traced in limited radar profiles connecting the Byrd and WAIS divide ice cores, where it was found at 68% and 80% of ice depth at Byrd and WD2014, respectively (Muldoon et al., 2018); however, they were also unable to recover deeper continuous IRHs more widely.

Overall, with the existing data sets available across the WAIS, the prospects for tracing and dating Holocene radiostratigraphy widely across the ice sheet with existing data are excellent, but diminish rapidly for older ice, going back to the LGM and beyond. Yet, much deeper, and thus older IRHs, are visible throughout the ice column with ground-based radars (e.g., Bingham et al., 2017; King, 2011; Laird et al., 2010) and hence the interrogation of older ice in the WAIS may be best suited to strategic ground campaigns that can be linked into the airborne-derived radiostratigraphy. In the PIG catchment, older ice is suggested by our results to lie below the PIG/Thwaites divide, where on average ~900 m of ice (30% of the mean ice thickness) underlies R4 (~17 ka) (Figure S5).

## 5. Conclusion

We have identified four spatially extensive IRHs in airborne radar surveys that are present across much of the Pine Island Glacier catchment in West Antarctica. Extending into neighboring Thwaites Glacier and Institute Ice Stream, these IRHs can be considered isochrones that span the late Pleistocene and Holocene, with ages of 2.31–2.92,  $4.72 \pm 0.28$ ,  $6.94 \pm 0.31$ , and  $16.50 \pm 0.79$  ka derived from intersecting the WAIS Divide Ice Core and the use of a 1-D ice-flow model. Our most spatially extensive IRH, R2, is remarkably similar in age and depth to another extensive IRH previously identified by other studies over Pine Island Glacier, Institute and Möller Ice Streams, and the Marie Byrd Land region. More broadly, we have also shown that our IRH package is similar to previously traced IRHs over the Weddell Sea sector of the WAIS, which, together with the Pine Island Glacier catchment represents ~20% of West Antarctica. Finally, we have shown that our upper three IRHs correspond to large peaks in sulfate concentrations at the WAIS Divide Ice Core, suggesting that our IRHs are of volcanic origin.

When assessing the presence of older ice across the catchment, we observe that the relative proportion of ice older than R4 in the ice column is limited and does not contain many continuous reflections. Indeed, we find that the deepest (and thus oldest) continuous IRH identified in this study, R4, is found at an average depth of 68% in the ice column despite its age (~17 ka), only representing 25% of the estimated age of the oldest ice recovered at the WAIS Divide Ice Core (~68 ka). This indicates that the majority of ice older than the LGM is found within the bottom ~30% of the ice thickness across PIG/Upper Thwaites. Whilst this is to be expected as the age-depth profile of an ice sheet does not increase linearly, the absence of continuous reflections dating back to the LGM and older currently limits our ability to reconstruct longer-term changes using existing airborne data sets.

As isochronous features, the dated IRHs generated here offer a new set of large-scale boundary conditions that could be a valuable resource, if incorporated into ice-flow models seeking to improve our understanding of past ice-sheet evolution. We anticipate that these well-dated IRHs will provide constraints for models simulating past accumulation rates and patterns, which in turn will shed more light onto the terrestrial ice sheet history of this very sensitive catchment of the WAIS.

## Data Availability Statement

The RACMO2 and MAR SMB outputs were downloaded from (<https://www.projects.science.uu.nl/iceclimate/publications/data/2018>) and (<https://zenodo.org/record/2547638>) respectively. Parts of the figures included in this study were produced with outputs from the Antarctic Mapping Toolbox in MATLAB® (Greene et al., 2017). The full picking information for each IRH can be downloaded from the UK Polar Data Center (<https://doi.org/10.5285/f2de31af-9f83-44f8-9584-f0190a2cc3eb>; Bodart et al., 2021).

## References

- Agosta, C., Amory, C., Kittel, C., Orsi, A., Favier, V., Gallée, H., et al. (2019). Estimation of the Antarctic surface mass balance using the regional climate model MAR (1979–2015) and identification of dominant processes. *The Cryosphere*, 13(1), 281–296. <https://doi.org/10.5194/tc-2018-76>
- Arthern, R. J., Winebrenner, D. P., & Vaughan, D. G. (2006). Antarctic snow accumulation mapped using polarization of 4.3-cm wavelength microwave emission. *The Journal of Geophysical Research*, 111(D6). <https://doi.org/10.1029/2004JD005667>
- Ashmore, D. W., Bingham, R. G., Ross, N., Siegert, M. J., Jordan, T. A., & Mair, D. W. F. (2020). Englacial architecture and age-depth constraints across the West Antarctic Ice Sheet. *Geophysical Research Letters*, 47. <https://doi.org/10.1029/2019GL086663>

## Acknowledgments

This study was motivated by the AntArchitecture Action Group of the Scientific Committee for Antarctic Research (SCAR). J. A. Bodart was supported by the NERC Doctoral Training Partnership grant (NE/L002558/1), hosted in the Edinburgh E<sup>3</sup> DTP program. The authors would like to thank the reviewers, Marie Cavitte and T. J. Fudge, for their constructive suggestions, which greatly improved this manuscript. The authors thank the BAS scientists and logistics personnel for acquiring the PASIN data over Pine Island Glacier, which will be made fully available upon publication from the Polar Airborne Geophysics Data Portal of the UK Polar Data Center (<https://secure.antarctica.ac.uk/data/aerogeo/>). The authors also thank CREsis for acquiring and providing the processed MCoRDS2 data, which can be downloaded from the OIB data portal (<https://data.cresis.ku.edu/>). The authors thank Brooke Medley and Howard Conway for providing the airborne and ground snow accumulation products.



- Bingham, R. G., Rippin, D. M., Karlsson, N. B., Corr, H. F. J., Ferraccioli, F., Jordan, T. A., et al. (2015). Ice-flow structure and ice dynamic changes in the Weddell Sea sector of West Antarctica from radar-imaged internal layering. *Journal of Geophysical Research: Earth Surface*, *120*(4), 655–670. <https://doi.org/10.1002/2014JF003291>
- Bingham, R. G., & Siegert, M. J. (2007). Radio-echo sounding over polar ice masses. *Journal of Environmental and Engineering Geophysics*, *12*(1), 47–62. <https://doi.org/10.2113/JEEG12.1.47>
- Bingham, R. G., Vaughan, D. G., King, E. C., Davies, D., Cornford, S. L., Smith, A. M., et al. (2017). Diverse landscapes beneath Pine Island Glacier influence ice flow. *Nature Communications*, *8*(1), 1618. <https://doi.org/10.1038/s41467-017-01597-y>
- Bodart, J. A., Bingham, R. G., Ashmore, D. W., Karlsson, N. B., Hein, A. S., & Vaughan, D. G. (2021). Dated radar stratigraphy of the Pine Island Glacier catchment (West Antarctica) derived from BBAS-PASIN (2004-05) and OIB-MCoRDS2 (2016/2018) surveys. UK Polar Data Centre, Natural Environment Research Council, UK Research & Innovation. <https://doi.org/10.5285/f2de31af-9f83-44f8-9584-f0190a2cc3eb>
- Bodart, J. A., & Bingham, R. J. (2019). The impact of the extreme 2015–2016 El Niño on the mass balance of the Antarctic Ice Sheet. *Geophysical Research Letters*, *46*(23), 13862–13871. <https://doi.org/10.1029/2019GL084466>
- Bracegirdle, T. J., Colleoni, F., Abram, N. J., Bertler, N. A. N., Dixon, D. A., England, M., et al. (2019). Back to the future: Using long-term observational and paleo-proxy reconstructions to improve model projections of Antarctic climate. *Geosciences*, *9*(6), 255. <https://doi.org/10.3390/geosciences9060255>
- Buizert, C., Cuffey, K. M., Severinghaus, J. P., Baggenstos, D., Fudge, T. J., Steig, E. J., et al. (2015). The WAIS Divide deep ice core WD2014 chronology – Part 1: Methane synchronization (68–31 ka BP) and the gas age–ice age difference. *Climate of the Past*, *11*(2), 153. <https://doi.org/10.5194/cp-11-153-2015>
- Castellano, E., Becagli, S., Hansson, M., Hutterli, M., Petit, J. R., Rampino, M. R., et al. (2005). Holocene volcanic history as recorded in the sulphate stratigraphy of the European Project for Ice Coring in Antarctica Dome C (EDC96) ice core. *Journal of Geophysical Research*, *110*(D6). <https://doi.org/10.1029/2004JD005259>
- Catania, G. A., Scambos, T. A., Conway, H., & Raymond, C. F. (2006). Sequential stagnation of Kamb Ice Stream, West Antarctica. *Geophysical Research Letters*, *33*(F1). <https://doi.org/10.1029/2006GL026430>
- Cavitte, M. G. P., Blankenship, D. D., Young, D. A., Schroeder, D. M., Parrenin, F., Lemeur, E., et al. (2016). Deep radiostratigraphy of the East Antarctic plateau: Connecting the Dome C and Vostok ice core sites. *Journal of Glaciology*, *62*(232), 323–334. <https://doi.org/10.1017/jog.2016.11>
- Cavitte, M. G. P., Dalaiden, Q., Goosse, H., Lenaerts, J. T. M., & Thomas, E. R. (2020). Reconciling the surface temperature–surface mass balance relationship in models and ice cores in Antarctica over the last 2 centuries. *The Cryosphere*, *14*, 4083–4102. <https://doi.org/10.5194/tc-14-4083-2020>
- Cavitte, M. G. P., Parrenin, F., Ritz, C., Young, D. A., Van Lieffering, B., Blankenship, D. D., et al. (2018). Accumulation patterns around Dome C, East Antarctica, in the last 73 kyr. *The Cryosphere*, *12*, 1401–1414. <https://doi.org/10.5194/tc-12-1401-2018>
- Christianson, K., Bushuk, M., Dutrieux, P., Parizek, B. R., Joughin, I. R., Alley, R. B., et al. (2016). Sensitivity of Pine Island Glacier to observed ocean forcing. *Geophysical Research Letters*, *43*(20), 10817–10825. <https://doi.org/10.1002/2016GL070500>
- Clough, J. W. (1977). Radio-echo sounding: Reflections from internal layers in ice sheets. *Journal of Glaciology*, *18*(78), 3–14. <https://doi.org/10.3189/S002214300002147X>
- Cole - Dai, J. (2014). “Major ion chemistry data of WAIS Divide ice core brittle ice”. U.S. Antarctic Program (USAP) Data Center. <https://doi.org/10.7265/N5RF5S0D>
- Corr, H. F. J., & Vaughan, D. G. (2008). A recent volcanic eruption beneath the West Antarctic Ice Sheet. *Nature Geoscience*, *1*(2), 122–125. <https://doi.org/10.1038/ngeo106>
- CReSIS (2016). CReSIS radar depth sounder data. Digital Media. Retrieved from <http://data.cresis.ku.edu/>
- Cuffey, K. M., Clow, G. D., Steig, E. J., Buizert, C., Fudge, T. J., Koutnik, M., et al. (2016). Deglacial temperature history of West Antarctica. *Proceedings of the National Academy of Sciences of the United States of America*, *113*(50), 14249–14254. <https://doi.org/10.1073/pnas.1609132113>
- Dalaiden, Q., Goosse, H., Klein, F., Lenaerts, J. T. M., Holloway, M., Sime, L., & Thomas, E. R. (2020). How useful is snow accumulation in reconstructing surface air temperature in Antarctica? A study combining ice core records and climate models. *The Cryosphere*, *14*(4), 1187. <https://doi.org/10.5194/tc-14-1187-2020>
- Dansgaard, W., & Johnsen, S. J. (1969). A flow model and a time scale for the ice core from Camp Century, Greenland. *Journal of Glaciology*, *8*(53), 215–223. <https://doi.org/10.3189/S002214300003120810.1017/s0022143000031208>
- DeConto, R. M., & Pollard, D. (2016). Contribution of Antarctica to past and future sea-level rise. *Nature*, *531*(7596), 591–597. <https://doi.org/10.1038/nature17145>
- Denton, G. H., & Hughes, T. J. (2002). Reconstructing the Antarctic ice sheet at the Last Glacial Maximum. *Quaternary Science Reviews*, *21*(1–3), 193–202. [https://doi.org/10.1016/S0277-3791\(01\)00090-7](https://doi.org/10.1016/S0277-3791(01)00090-7)
- Dutrieux, P., De Rydt, J., Jenkins, A., Holland, P. R., Ha, H. K., Lee, S. H., et al. (2014). Strong sensitivity of Pine Island ice-shelf melting to climatic variability. *Science*, *343*(6167), 174–178. <https://doi.org/10.1126/science.1244341>
- Eisen, O., Frezzotti, M., Genthon, C., Isaksson, E., Magand, O., van den Broeke, M. R., et al. (2008). Ground-based measurements of spatial and temporal variability of snow accumulation in East Antarctica. *Reviews of Geophysics*, *46*(2). <https://doi.org/10.1029/2006RG000218>
- Eisen, O., Rack, W., Nixdorf, U., & Wilhelms, F. (2005). Characteristics of accumulation around the EPICA deep-drilling site in Dronning Maud Land, Antarctica. *Annals of Glaciology*, *41*, 41–46. <https://doi.org/10.3189/172756405781813276>
- Fahnestock, M., Abdalati, W., Joughin, I., Brozena, J., & Gogineni, P. (2001). High geothermal heat flow, basal melt, and the origin of rapid ice flow in central Greenland. *Science*, *294*(5550), 2338–2342. <https://doi.org/10.1126/science.1065370>
- Fahnestock, M., Abdalati, W., Luo, S., & Gogineni, S. (2001). Internal layer tracing and age–depth–accumulation relationships for the northern Greenland ice sheet. *Journal of Geophysical Research*, *106*(D24), 33789–33797. <https://doi.org/10.1029/2001JD900200>
- Favier, L., Durand, G., Cornford, S. L., Gudmundsson, G. H., Gagliardini, O., Gillet-Chaulet, F., et al. (2014). Retreat of Pine Island Glacier controlled by marine ice-sheet instability. *Nature Climate Change*, *4*(2), 117. <https://doi.org/10.1038/nclimate2094>
- Fudge, T. J., Biyani, S. C., Clemens-Sewall, D., & Hawley, R. L. (2019). Constraining geothermal flux at coastal domes of the Ross Ice Sheet, Antarctica. *Geophysical Research Letters*, *46*(22), 13090–13098. <https://doi.org/10.1029/2019GL084332>
- Fudge, T. J., Markle, B. R., Cuffey, K. M., Buizert, C., Taylor, K. C., Steig, E. J., et al. (2016). Variable relationship between accumulation and temperature in West Antarctica for the past 31,000 years. *Geophysical Research Letters*, *43*(8), 3795–3803. <https://doi.org/10.1002/2016GL068356>
- Fujita, S., Maeno, H., Uratsuka, S., Furukawa, T., Mae, S., Fujii, Y., & Watanabe, O. (1999). Nature of radio echo layering in the Antarctic Ice Sheet detected by a two-frequency experiment. *Journal of Geophysical Research*, *104*(B6), 13013–13024. <https://doi.org/10.1029/1999JB900034>

- Fujita, S., Matsuoka, T., Ishida, T., Matsuoka, K., & Mae, S. (2000). A summary of the complex dielectric permittivity of ice in the megahertz range and its applications for radar sounding of polar ice sheets. In T. Hondoh (Ed.), *Physics of ice core records* (pp. 185–212). Hokkaido University Press.
- Golledge, N. R., Menviel, L., Carter, L., Fogwill, C. J., England, M. H., Cortese, G., & Levy, R. H. (2014). Antarctic contribution to meltwater pulse 1A from reduced Southern Ocean overturning. *Nature Communications*, 5, 5107. <https://doi.org/10.1038/ncomms6107>
- Gow, A. J. (1970). Preliminary results of studies of ice cores from the 2164m-deep drill hole, Byrd Station, Antarctica. Paper presented at the international symposium on Antarctic Glaciological Exploration, IAHS Publication (Vol. 86 (pp. 78–90)). IAHS.
- Gow, A. J., & Williamson, T. (1971). Volcanic ash in the Antarctic ice sheet and its possible climatic implications. *Earth and Planetary Science Letters*, 13(1), 210–218. [https://doi.org/10.1016/0012-821X\(71\)90126-9](https://doi.org/10.1016/0012-821X(71)90126-9)
- Greene, C. A., Gwyther, D. E., & Blankenship, D. D. (2017). Antarctic mapping tools for Matlab. *Computers & Geosciences*, 104, 151–157. <https://doi.org/10.1016/j.cageo.2016.08.003>
- Hammer, C. U., Clausen, H. B., & Langway, C. C., Jr. (1997). 50,000 years of recorded global volcanism. *Climatic Change*, 35(1), 1–15. <https://doi.org/10.1023/A:1005344225434>
- Harrison, C. H. (1973). Radio echo sounding of horizontal layers in ice. *Journal of Glaciology*, 12(66), 383–397. <https://doi.org/10.3189/S0022143000031804>
- Hillenbrand, C.-D., Kuhn, G., Smith, J. A., Gohl, K., Graham, A. G. C., Larter, R. D., et al. (2013). Grounding-line retreat of the west Antarctic ice sheet from inner Pine Island Bay. *Geology*, 41(1), 35–38. <https://doi.org/10.1130/G33469.1>
- Holland, P. R., Bracegirdle, T. J., Dutrieux, P., Jenkins, A., & Steig, E. J. (2019). West Antarctic ice loss influenced by internal climate variability and anthropogenic forcing. *Nature Geoscience*, 12(9), 718–724. <https://doi.org/10.1038/s41561-019-0420-9>
- Holschuh, N., Christianson, K., & Anandakrishnan, S. (2014). Power loss in dipping internal reflectors, imaged using ice-penetrating radar. *Annals of Glaciology*, 55(67), 49–56. <https://doi.org/10.3189/2014AoG67A005>
- Holschuh, N., Christianson, K., Conway, H., Jacobel, R. W., & Welch, B. C. (2018). Persistent tracers of historic ice flow in glacial stratigraphy near Kamb Ice Stream, West Antarctica. *The Cryosphere*, 12(9), 2821–2829. <https://doi.org/10.5194/tc-12-2821-2018>
- Jacobel, R. W., Scambos, T. A., Raymond, C. F., & Gades, A. M. (1996). Changes in the configuration of ice stream flow from the West Antarctic Ice Sheet. *Journal of Geophysical Research*, 101(B3), 5499–5504. <https://doi.org/10.1029/95JB03735>
- Jacobel, R. W., & Welch, B. C. (2005). A time marker at 17.5 kyr BP detected throughout West Antarctica. *Annals of Glaciology*, 41, 47–51. <https://doi.org/10.3189/172756405781813348>
- Jakobsson, M., Anderson, J. B., Nitsche, F. O., Dowdeswell, J. A., Gyllencreutz, R., Kirchner, N., et al. (2011). Geological record of ice shelf break-up and grounding line retreat, Pine Island Bay, West Antarctica. *Geology*, 39(7), 691–694. <https://doi.org/10.1130/G32153.1>
- Johnson, J. S., Bentley, M. J., & Gohl, K. (2008). First exposure ages from the Amundsen Sea embayment, West Antarctica: The late Quaternary context for recent thinning of Pine Island, Smith, and Pope Glaciers. *Geology*, 36(3), 223–226. <https://doi.org/10.1130/G24207A.1>
- Johnson, J. S., Bentley, M. J., Smith, J. A., Finkel, R. C., Rood, D. H., Gohl, K., et al. (2014). Rapid thinning of Pine Island Glacier in the early Holocene. *Science*, 343(6174), 999–1001. <https://doi.org/10.1126/science.1247385>
- Johnson, J. S., Roberts, S. J., Rood, D. H., Pollard, D., Schaefer, J. M., Whitehouse, P. L., et al. (2020). Deglaciation of Pope Glacier implies widespread early Holocene ice sheet thinning in the Amundsen Sea sector of Antarctica. *Earth and Planetary Science Letters*, 548, 116501. <https://doi.org/10.1016/j.epsl.2020.116501>
- Johnson, J. S., Smith, J. A., Schaefer, J. M., Young, N. E., Goehring, B. M., Hillenbrand, C.-D., et al. (2017). The last glaciation of Bear Peninsula, central Amundsen Sea Embayment of Antarctica: Constraints on timing and duration revealed by in situ cosmogenic <sup>14</sup>C and <sup>10</sup>Be dating. *Quaternary Science Reviews*, 178, 77–88. <https://doi.org/10.1016/j.quascirev.2017.11.003>
- Karlsson, N. B., Bingham, R. G., Rippin, D. M., Hindmarsh, R. C. A., Corr, H. F. J., & Vaughan, D. G. (2014). Constraining past accumulation in the central Pine Island Glacier basin, West Antarctica, using radio-echo sounding. *Journal of Glaciology*, 60(221), 553–562. <https://doi.org/10.3189/2014JoG13j180>
- Karlsson, N. B., Rippin, D. M., Bingham, R. G., & Vaughan, D. G. (2012). A 'continuity-index' for assessing ice-sheet dynamics from radar-sounded internal layers. *Earth and Planetary Science Letters*, 335–336, 88–94. <https://doi.org/10.1016/j.epsl.2012.04.034>
- Karlsson, N. B., Rippin, D. M., Vaughan, D. G., & Corr, H. F. J. (2009). The internal layering of Pine Island Glacier, West Antarctica, from airborne radar-sounding data. *Annals of Glaciology*, 50(51), 141–146. <https://doi.org/10.3189/S0260305500250660>
- King, E. C. (2011). Ice stream or not? Radio-echo sounding of Carlson Inlet, West Antarctica. *The Cryosphere*, 5(4), 907–916. <https://doi.org/10.5194/tc-5-907-2011>
- King, E. C. (2020). The precision of radar-derived subglacial bed topography: A case study from Pine Island Glacier, Antarctica. *Annals of Glaciology*, 61, 154–161. <https://doi.org/10.1017/aog.2020.33>
- Kingslake, J., Scherer, R. P., Albrecht, T., Coenen, J., Powell, R. D., Reese, R., et al. (2018). Extensive retreat and re-advance of the West Antarctic Ice Sheet during the Holocene. *Nature*, 558(7710), 430. <https://doi.org/10.1038/s41586-018-0208-x>
- Konrad, H., Gilbert, L., Cornford, S. L., Payne, A., Hogg, A., Muir, A., & Shepherd, A. (2017). Uneven onset and pace of ice-dynamical imbalance in the Amundsen Sea Embayment, West Antarctica. *Geophysical Research Letters*, 44(2), 910–918. <https://doi.org/10.1002/2016GL070733>
- Koutnik, M. R., Fudge, T. J., Conway, H., Waddington, E. D., Neumann, T. A., Cuffey, K. M., et al. (2016). Holocene accumulation and ice flow near the West Antarctic Ice Sheet Divide ice core site. *Journal of Geophysical Research: Earth Surface*, 121(5), 907–924. <https://doi.org/10.1002/2015JF003668>
- Laird, C. M., Blake, W. A., Matsuoka, K., Conway, H., Allen, C. T., Leuschen, C. J., & Gogineni, S. (2010). Deep ice stratigraphy and basal conditions in central West Antarctica revealed by coherent radar. *IEEE Geoscience and Remote Sensing Letters*, 7(2), 246–250. <https://doi.org/10.1109/LGRS.2009.2032304>
- Lenaerts, J. T. M., Van den Broeke, M. R., Van de Berg, W. J., Van Meijgaard, E., & Kuipers Munneke, P. (2012). A new, high-resolution surface mass balance map of Antarctica (1979–2010) based on regional atmospheric climate modeling. *Geophysical Research Letters*, 39(4). <https://doi.org/10.1029/2011GL050713>
- Laysinger Vieli, G. J.-M. C., Hindmarsh, R. C. A., Siegert, M. J., & Bo, S. (2011). Time-dependence of the spatial pattern of accumulation rate in East Antarctica deduced from isochronous radar layers using a 3-D numerical ice flow model. *Journal of Geophysical Research*, 116(F2). <https://doi.org/10.1029/2010JF001785>
- Lindow, J., Castex, M., Wittmann, H., Johnson, J. S., Lisker, F., Gohl, K., & Spiegel, C. (2014). Glacial retreat in the Amundsen Sea sector, West Antarctica – First cosmogenic evidence from central Pine Island Bay and the Kohler Range. *Quaternary Science Reviews*, 98, 166–173. <https://doi.org/10.1016/j.quascirev.2014.05.010>
- Lliboutry, L. A. (1979). A critical review of analytical approximate solutions for steady state velocities and temperatures in cold ice sheets. *Zeitschr Gletscherkde Glazialgeology*, 15, 135–148.

- Lowe, A. L., & Anderson, J. B. (2002). Reconstruction of the West Antarctic ice sheet in Pine Island Bay during the Last Glacial Maximum and its subsequent retreat history. *Quaternary Science Reviews*, 21(16–17), 1879–1897. [https://doi.org/10.1016/S0277-3791\(02\)00006-9](https://doi.org/10.1016/S0277-3791(02)00006-9)
- MacGregor, J. A., Colgan, W. T., Fahnestock, M. A., Morlighem, M., Catania, G. A., Paden, J. D., & Gogineni, S. P. (2016). Holocene deceleration of the Greenland ice sheet. *Science*, 351(6273), 590–593. <https://doi.org/10.1126/science.aab1702>
- MacGregor, J. A., Fahnestock, M. A., Catania, G. A., Paden, J. D., Prasad Gogineni, S., Young, S. K., et al. (2015). Radiostratigraphy and age structure of the Greenland Ice Sheet. *Journal of Geophysical Research: Earth Surface*, 120(2), 212–241. <https://doi.org/10.1002/2014JF003215>
- McConnell, J. R., Burke, A., Dunbar, N. W., Köhler, P., Thomas, J. L., Arienzo, M. M., et al. (2017). Synchronous volcanic eruptions and abrupt climate change ~17.7 ka plausibly linked by stratospheric ozone depletion. *Proceedings of the National Academy of Sciences of the United States of America*, 114(38), 10035–10040. <https://doi.org/10.1073/pnas.1705595114>
- Medley, B., Joughin, I., Smith, B. E., Das, S. B., Steig, E. J., Conway, H., et al. (2014). Constraining the recent mass balance of Pine Island and Thwaites glaciers, West Antarctica, with airborne observations of snow accumulation. *The Cryosphere*, 8, 1375–1392. <https://doi.org/10.5194/tc-8-1375-2014>
- Medley, B., McConnell, J. R., Neumann, T. A., Reijmer, C. H., Chellman, N., Sigl, M., & Kipfstuhl, S. (2018). Temperature and snowfall in western Queen Maud Land increasing faster than climate model projections. *Geophysical Research Letters*, 45(3), 1472–1480. <https://doi.org/10.1002/2017GL075992>
- Millar, D. H. M. (1981). Radio-echo layering in polar ice sheets and past volcanic activity. *Nature*, 292(5822), 441–443. <https://doi.org/10.1038/292441a0>
- Millar, D. H. M. (1982). Acidity levels in ice sheets from radio echo-sounding. *Annals of Glaciology*, 3, 199–203. <https://doi.org/10.3189/S026030550000277910.1017/s0260305500002779>
- Moore, J. C. (1988). Dielectric variability of a 130 m Antarctic ice core: Implications for radar sounding. *Annals of Glaciology*, 11, 95–99. <https://doi.org/10.3189/S026030550000639X>
- Morlighem, M., Rignot, E., Binder, T., Blankenship, D., Drews, R., Eagles, G., et al. (2020). Deep glacial troughs and stabilizing ridges unveiled beneath the margins of the Antarctic ice sheet. *Nature Geoscience*, 13(2), 132–137. <https://doi.org/10.1038/s41561-019-0510-8>
- Muldoon, G. R. (2018). West Antarctic ice sheet retreat during the last interglacial (Doctoral dissertation). The University of Texas at Austin ScholarWorks Repository. <https://doi.org/10.15781/T23B5WS0D>
- Muldoon, G. R., Jackson, C. S., Young, D. A., & Blankenship, D. D. (2018). Bayesian estimation of englacial radar chronology in Central West Antarctica. *Dynamics and Statistics of the Climate System*, 3(1), dzy004. <https://doi.org/10.1093/climatesystem/dzy004>
- Neumann, T. A., Conway, H., Price, S. F., Waddington, E. D., Catania, G. A., & Morse, D. L. (2008). Holocene accumulation and ice sheet dynamics in central West Antarctica. *Journal of Geophysical Research*, 113(F2). <https://doi.org/10.1029/2007JF000764>
- Nielsen, L. T., Aðalgeirsdóttir, G., Gkinis, V., Nuterman, R., & Hvidberg, C. S. (2018). The effect of a Holocene climatic optimum on the evolution of the Greenland ice sheet during the last 10 kyr. *Journal of Glaciology*, 64(245), 477–488. <https://doi.org/10.1017/jog.2018.40>
- Nye, J. F. (1957). The distribution of stress and velocity in glaciers and ice-sheets. *Proceedings of the Royal Society of London - Series A: Mathematical and Physical Sciences*, 239(1216), 113–133. <https://doi.org/10.1098/rspa.1957.0026>
- Palermé, C., Genthon, C., Claud, C., Kay, J. E., Wood, N. B., & L'Ecuyer, T. (2017). Evaluation of current and projected Antarctic precipitation in CMIP5 models. *Climate Dynamics*, 48(1–2), 225–239. <https://doi.org/10.1007/s00382-016-3071-1>
- Parrenin, F., Cavitte, M. G. P., Blankenship, D. D., Chappellaz, J., Fischer, H., Gagliardini, O., et al. (2017). Is there 1.5-million-year-old ice near Dome C, Antarctica? *The Cryosphere*, 11(6), 2427–2437. <https://doi.org/10.5194/tc-11-2427-2017>
- Rignot, E., Mouginot, J., & Scheuchl, B. (2017). MEaSUREs InSAR-based Antarctica ice velocity map, version 2. NASA National Snow and Ice Data Center Distributed Active Archive Center. <https://doi.org/10.5067/D7GK8F5J8M8R>
- Rignot, E., Mouginot, J., Scheuchl, B., van den Broeke, M., van Wessem, M. J., & Morlighem, M. (2019). Four decades of Antarctic Ice Sheet mass balance from 1979–2017. *Proceedings of the National Academy of Sciences of the United States of America*, 116(4), 1095–1103. <https://doi.org/10.1073/pnas.1812883116>
- Ritz, C., Rommelaere, V., & Dumas, C. (2001). Modeling the evolution of Antarctic ice sheet over the last 420,000 years: Implications for altitude changes in the Vostok region. *Journal of Geophysical Research*, 106(D23), 31943–31964. <https://doi.org/10.1029/2001JD900232>
- Ross, N., Corr, H., & Siegert, M. (2020). Large-scale englacial folding and deep-ice stratigraphy within the West Antarctic Ice Sheet. *The Cryosphere*, 14, 2103–2114. <https://doi.org/10.5194/tc-14-2103-2020>
- Rotschky, G., Eisen, O., Wilhelms, F., Nixdorf, U., & Oerter, H. (2004). Spatial distribution of surface mass balance on Amundsenisen plateau, Antarctica, derived from ice-penetrating radar studies. *Annals of Glaciology*, 39, 265–270. <https://doi.org/10.3189/172756404781814618>
- Scambos, T. A., Haran, T. M., Fahnestock, M. A., Painter, T. H., & Bohlander, J. (2007). MODIS-based Mosaic of Antarctica (MOA) data sets: Continent-wide surface morphology and snow grain size. *Remote Sensing of Environment*, 111(2–3), 242–257. <https://doi.org/10.1016/j.rse.2006.12.020>
- Shepherd, A., Ivins, E. R., Rignot, E., Smith, B., Van Den Broeke, M., Velicogna, I., et al. (2018). Mass balance of the Antarctic Ice Sheet from 1992 to 2017. *Nature*, 556, 219–222. <https://doi.org/10.1038/s41586-018-0179-y>
- Siegert, M. J., Hodgkins, R., & Dowdeswell, J. A. (1998). A chronology for the Dome C deep ice-core site through radio-echo layer Correlation with the Vostok Ice Core, Antarctica. *Geophysical Research Letters*, 25(7), 1019–1022. <https://doi.org/10.1029/98GL00718>
- Siegert, M. J., & Payne, A. J. (2004). Past rates of accumulation in central West Antarctica. *Geophysical Research Letters*, 31(12). <https://doi.org/10.1029/2004GL020290>
- Siegert, M. J., Pokar, M., Dowdeswell, J. A., & Benham, T. (2005). Radio-echo layering in West Antarctica: A spreadsheet dataset. *Earth Surface Processes and Landforms*, 30(12), 1583–1591. <https://doi.org/10.1002/esp.1238>
- Sigl, M., Fudge, T. J., Winstrup, M., Cole-Dai, J., Ferris, D., McConnell, J. R., et al. (2016). The WAIS Divide deep ice core WD2014 chronology – Part 2: Annual-layer counting (0–31 ka BP). *Climate of the Past*, 12(3), 769–786. <https://doi.org/10.5194/cp-12-769-2016>
- Smith, J. A., Andersen, T. J., Shortt, M., Gaffney, A. M., Truffer, M., Stanton, T. P., et al. (2017). Sub-ice-shelf sediments record history of twentieth-century retreat of Pine Island Glacier. *Nature*, 541(7635), 77–80. <https://doi.org/10.1038/nature20136>
- Steinhage, D., Kipfstuhl, S., Nixdorf, U., & Miller, H. (2013). Internal structure of the ice sheet between Kohnen station and Dome Fuji, Antarctica, revealed by airborne radio-echo sounding. *Annals of Glaciology*, 54(64), 163–167. <https://doi.org/10.3189/2013AoG64A113>
- van Wessem, J. M., van de Berg, W. J., Noël, B. P. Y., Van Meijgaard, E., Amory, C., Birnbaum, G., et al. (2018). Modeling the climate and surface mass balance of polar ice sheets using RACMO2 – Part 2: Antarctica (1979–2016). *The Cryosphere*, 12(4), pp.1479–1498. <https://doi.org/10.5194/tc-12-1479-2018>
- Vaughan, D. G., Corr, H. F. J., Ferraccioli, F., Frearson, N., O'Hare, A., Mach, D., et al. (2006). New boundary conditions for the West Antarctic ice sheet: Subglacial topography beneath Pine Island Glacier. *Geophysical Research Letters*, 33(9). <https://doi.org/10.1029/2005GL025588>

- Waddington, E. D., Conway, H., Steig, E. J., Alley, R. B., Brook, E. J., Taylor, K. C., & White, J. W. C. (2005). Decoding the dipstick: Thickness of Siple Dome, West Antarctica, at the last glacial maximum. *Geology*, 33(4), 281–284. <https://doi.org/10.1130/G21165.1>
- Waddington, E. D., Neumann, T. A., Koutnik, M. R., Marshall, H.-P., & Morse, D. L. (2007). Inference of accumulation-rate patterns from deep layers in glaciers and ice sheets. *Journal of Glaciology*, 53(183), 694–712. <https://doi.org/10.3189/002214307784409351>
- Wang, Y., Ding, M., Van Wessem, J. M., Schlosser, E., Altnau, S., van den Broeke, M. R., et al. (2016). A comparison of Antarctic Ice Sheet surface mass balance from atmospheric climate models and in situ observations. *Journal of Climate*, 29(14), 5317–5337. <https://doi.org/10.1175/JCLI-D-15-0642.1>
- Whillans, I. M. (1976). Radio-echo layers and the recent stability of the West Antarctic ice sheet. *Nature*, 264(5582), 152–155. <https://doi.org/10.1038/264152a0>
- Winter, A., Steinhage, D., Arnold, E. J., Blankenship, D. D., Cavitte, M. G. P., Corr, H. F. J., et al. (2017). Comparison of measurements from different radio-echo sounding systems and synchronization with the ice core at Dome C, Antarctica. *The Cryosphere*, 11(1), 653–668. <https://doi.org/10.5194/tc-11-653-2017>
- Winter, A., Steinhage, D., Creyts, T. T., Kleiner, T., & Eisen, O. (2019). Age stratigraphy in the East Antarctic Ice Sheet inferred from radio-echo sounding horizons. *Earth System Science Data*, 11(3), 1069–1081. <https://doi.org/10.5194/essd-11-1069-2019>
- Zwally, H. J., Giovinetto, M. B., Beckley, M. A., & Saba, J. L. (2012). Antarctic and Greenland drainage systems. Retrieved from GSFC Cryospheric Sciences Laboratory. [https://icesat4.gsfc.nasa.gov/cryo\\_data/ant\\_grn\\_drainage\\_systems.php](https://icesat4.gsfc.nasa.gov/cryo_data/ant_grn_drainage_systems.php)

## References From the Supporting Information

- Conway, H., & Rasmussen, L. A. (2009). Recent thinning and migration of the Western Divide, central West Antarctica. *Geophysical Research Letters*, 36, L12502. <https://doi.org/10.1029/2009GL038072>
- Dowdeswell, J. A., & Evans, S. (2004). Investigations of the form and flow of ice sheets and glaciers using radio-echo sounding. *Reports on Progress in Physics*, 67(10), 1821. <https://doi.org/10.1088/0034-4885/67/10/R03>
- Hein, A. S., Woodward, J., Marrero, S. M., Dunning, S. A., Steig, E. J., Freeman, S. P. H. T., et al. (2016). Evidence for the stability of the West Antarctic Ice Sheet divide for 1.4 million years. *Nature Communications*, 7(1), 1–8. <https://doi.org/10.1038/ncomms10325>
- Ross, N., Bingham, R. G., Corr, H. F. J., Ferraccioli, F., Jordan, T. A., Le Brocq, A., et al. (2012). Steep reverse bed slope at the grounding line of the Weddell Sea sector in West Antarctica. *Nature Geoscience*, 5, 393–396. <https://doi.org/10.1038/ngeo1468>
- Ross, N., Siegert, M. J., Woodward, J., Smith, A. M., Corr, H. F. J., Bentley, M. J., et al. (2011). Holocene stability of the Amundsen-Weddell ice divide, West Antarctica. *Geology*, 39(10), 935–938. <https://doi.org/10.1130/G3192010.1130/g31920.1>
- Schroeder, D. M., Dowdeswell, J. A., Siegert, M. J., Bingham, R. G., Chu, W., MacKie, E. J., et al. (2019). Multidecadal observations of the Antarctic ice sheet from restored analog radar records. *Proceedings of the National Academy of Sciences of the United States of America*, 116(38), 18867–18873. <https://doi.org/10.1073/pnas.1821646116>
- Schwander, J., Jouzel, J., Hammer, C. U., Petit, J.-R., Udisti, R., & Wolff, E. (2001). A tentative chronology for the EPICA Dome Concordia ice core. *Geophysical Research Letters*, 28(22), 4243–4246. <https://doi.org/10.1029/2000GL011981>
- Siegert, M. J., Ross, N., Corr, H., Kingslake, J., & Hindmarsh, R. (2013). Late Holocene ice-flow reconfiguration in the Weddell Sea sector of West Antarctica. *Quaternary Science Reviews*, 78, 98–107. <https://doi.org/10.1016/j.quascirev.2013.08.003>

*Journal of Geophysical Research: Earth Surface*

Supporting Information to

**Age-Depth Stratigraphy of Pine Island Glacier Inferred from Airborne Radar and Ice-Core Chronology**

J. A. Bodart<sup>1,4\*</sup>, R. G. Bingham<sup>1</sup>, D. W. Ashmore<sup>2</sup>, N. B. Karlsson<sup>3</sup>, A.S. Hein<sup>1</sup>, and D. G. Vaughan<sup>4</sup>

<sup>1</sup> School of GeoSciences, University of Edinburgh, Edinburgh, UK.

<sup>2</sup> School of Environmental Sciences, University of Liverpool, Liverpool, UK.

<sup>3</sup> Geological Survey of Denmark and Greenland, Copenhagen, Denmark.

<sup>4</sup> British Antarctic Survey, Cambridge, UK.

\*Corresponding author: Julien Bodart ([julien.bodart@ed.ac.uk](mailto:julien.bodart@ed.ac.uk))

**Content of this file**

**Figure S1.** Radargram and radar trace profile showing IRH characteristics and return power.

**Figure S2.** Map showing the spatial extent of IRHs R1-4 across our study area (grey lines) and selected crossover points for IRHs traced on PIG-PASIN and OIB-MCoRDS2.

**Table S1.** Crossover depth analysis for ten locations (I1-10, Figure S2) where R1-4 intersect each other at flightpath crossovers on the PIG-PASIN data.

**Table S2.** Crossover depth analysis for five locations (K1-5, Figure S2) where R4 traced on the OIB-MCoRDS2 data (this study) intersects the  $17.5 \pm 0.5$  ka layer (Jacobel and Welch, 2005).

**Text S1.** Radar-depth Uncertainties

**Text S2.** Age-depth Modelling Calculations

**Table S3.** IRH depths (m) at three locations where the SPRI/NSF/TUD survey intersects the PIG-PASIN survey.

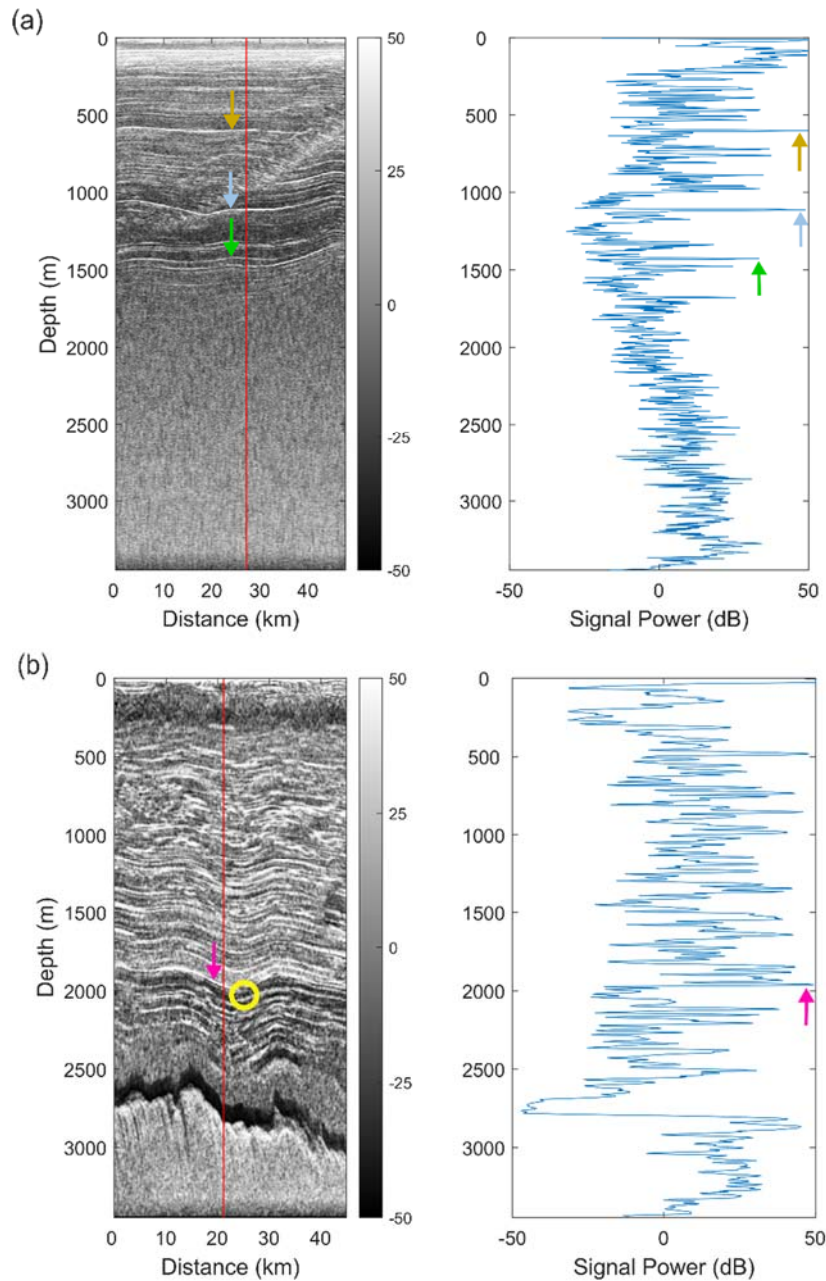
**Table S4.** Accumulation rates ( $\text{m a}^{-1}$ ) for each IRH at Site A and B, as calculated using the four accumulation datasets mentioned in the main text (see 2.4.2).

**Additional Figures:**

**Figure S3.** Comparison between our IRHs and Karlsson et al. (2014) and Ashmore et al.'s (2020) IRHs.

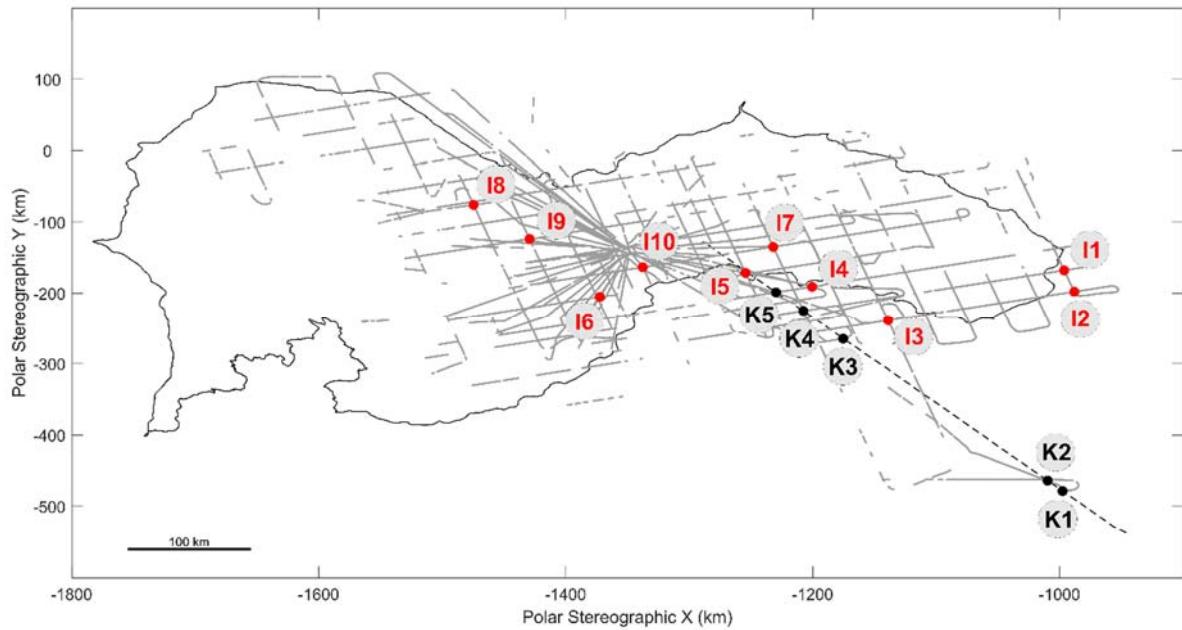
**Figure S4.** Sulphate concentration ( $\mu\text{g/kg}$ ) as a function of depth (m) at the WAIS Divide ice-core site for: (a) the brittle section of the WDC06A ice core (577-1300 m) from Cole-Dai (2014); and (b) for depths of 1300-3404 m at WD2014 ice core from McConnell (2017).

**Figure S5.** Ice thickness (m) below R3 (a) and R4 (b) traced over the PIG-PASIN and OIB-MCoRDS2 data.



53  
54  
55  
56  
57  
58  
59  
60  
61

**Figure S1.** Radargram and radar trace profile showing IRH characteristics and return power on the PIG-PASIN data. Colours of arrows are per legend in Figure 2a of the main manuscript. (a) Pulse radargram along the control line (segment AA-AB, Figure 1-2 of main manuscript) showing IRHs R1-3 and their peak power, with R1 (yellow), R2 (blue), R3 (green). The red line on the radargram shows the location of the radar trace. (b) Same as for (a) but on PIG-PASIN flight line 1 (chirp mode) with R4 (pink) shown as well as the depth and location of where Jacobel and Welch's (2005)  $17.5 \pm 0.5$  ka layer (yellow circle) intersects our data.



62  
63 **Figure S2.** Map showing the spatial extent of IRHs R1-4 across our study area (grey lines) and selected crossover  
64 points for IRHs traced on PIG-PASIN and OIB-MCoRDS2. The red dots I1-10 show the ten intersections where  
65 we directly compare the depth of IRHs R1-4 traced on the PIG-PASIN data. The black dots K1-5 are where we  
66 directly compare the depths of R4 (this study) with the depth of the  $17.5 \pm 0.5$  ka layer (Jacobel and Welch, 2005).  
67 The black dotted line is where Jacobel and Welch's (2005) profile intersects our dataset. The black outline in the  
68 background is the ICESat IMBIE basin containing the Pine Island Glacier (Zwally et al., 2012).

69  
70  
71 **Table S1.** Crossover depth analysis for ten locations (I1-10, Figure S2) where R1-4 intersect each other at  
72 flightpath crossovers on the PIG-PASIN data. Depth uncertainty for PIG-PASIN is  $\pm 17$  m.  
73

	<i>IRH</i>	<i>Depths at intersection (m)</i>			<i>IRH</i>	<i>Depths at intersection (m)</i>	
<b>I1</b>	R1	467	470	<b>I6</b>	R1	816	814
	R2	890	896		R2	1488	1503
	R3	1193	1197		R3	1592	1596
	R4	-	-		R4	-	-
<b>I2</b>	R1	525	503	<b>I7</b>	R1	723	728
	R2	947	942		R2	1099	1100
	R3	1286	1284		R3	1410	1412
	R4	2086	2085		R4	-	-
<b>I3</b>	R1	532	537	<b>I8</b>	R1	559	558
	R2	1181	1176		R2	802	806
	R3	1483	1479		R3	989	1004
	R4	2021	2016		R4	-	-
<b>I4</b>	R1	796	797	<b>I9</b>	R1	599	598
	R2	1223	1224		R2	958	954
	R3	1499	1502		R3	1161	1160
	R4	2072	2058		R4	-	-
<b>I5</b>	R1	-	-	<b>I10</b>	R1	956	946
	R2	1488	1503		R2	1577	1576
	R3	1796	1797		R3	2010	1993
	R4	2197	2192		R4	-	-

74

75 **Table S2.** Crossover depth analysis for five locations (K1-5, Figure S2) where R4 traced on the OIB-MCoRDS2  
 76 data (this study) intersects the  $17.5 \pm 0.5$  ka layer (Jacobel and Welch, 2005). Depth uncertainty for the OIB-  
 77 MCoRDS2 IRH is  $\pm 14$  m. Estimated uncertainty for the  $17.5 \pm 0.5$  ka layer from Jacobel and Welch (2005) is  $\pm$   
 78 10 m.

	<i>Depths at intersection (m)</i>	
	Jacobel and Welch (2005)	This Study
K1	1439	1424
K2	1848	1824
K3	1784	1764
K4	1725	1743
K5	1917	1905

79

80 **Text S1: Radar-depth Uncertainties**

81

82 There are three main sources of uncertainties when imaging IRHs with ice-penetrating  
 83 radars: the speed of the electromagnetic wave through ice, uncertainties with the firm correction,  
 84 and the range resolution of the radar system. We describe these in more details here.

85

86 The greatest source of uncertainty when calculating the depth of an IRH is the true  
 87 speed of electromagnetic wave in the ice, which varies due to ice properties and is limited by  
 88 a lack of detailed observations of ice properties with depth. This value depends on impurity  
 89 concentrations, anisotropy and temperature, and ranges from  $p =$   
 90  $(v_{ice}) \sim U [168.0, 169.5] m \mu s^{-1}$  (Fujita et al., 2000). Because this error increases with depth,  
 91 the maximum uncertainty can be found on the deepest IRH. Values for this uncertainty are  
 92 provided in the main text (see Section 2.3 of the main manuscript).

93

94 The radar signal travels at a faster rate in the lower-density firm ( $\sim 350$ - $900 \text{ kg m}^{-3}$ ) than  
 95 in the higher-density solid ice ( $\sim 917 \text{ kg m}^{-3}$ ). To correct for this, radar studies typically  
 96 calculate a spatially-invariant firm correction  $Z_f$  and add this value in the vertical direction  
 97 (Equation 1 in the main text) (Dowdeswell and Evans, 2004). Previous studies over West  
 98 Antarctica (i.e. Ross et al., 2012; Siegert et al., 2013) used a value of  $Z_f = 10 \text{ m}$ , based on the  
 99 high-resolution density profiles at WAIS Divide (see Ashmore et al., 2020). Since our IRHs  
 100 are in close proximity to the WD2014 site, we also use this nominal value of 10 m and apply it  
 101 to all our IRHs. We estimate the uncertainty associated with the firm correction to be  $\pm 3 \text{ m}$ ,  
 102 owing to minor variations in firm densification across the catchment (see Ashmore et al., 2020  
 103 for details).

104

105 The range resolution, or vertical resolution represents the ability of a radar system to  
 106 detect between two closely-spaced targets with similar reflection strengths. Denoted  $\Delta r$ , it is  
 107 given by the bandwidth of a chirped radar system,  $B$ , the dielectric constant of ice,  $\epsilon' = 3.17$ ,  
 108 the speed of light in a vacuum,  $c_0$ , and a window widening factor,  $k$ , of 1.53 for 20% Tukey  
 109 time-domain, as per CReSIS (2016). This results in the following equation:

$$110 \quad \Delta r = \frac{kc_0}{2B\sqrt{\epsilon'}} \quad (S1)$$

111 We calculate the range resolution for each system, with values given in the main text  
 112 and in Table 1 of the main manuscript. The SNR for each reflector for a point target is a function  
 113 of the reflector signal power and noise power, as per Cavitt et al. (2016). It is used alongside



114 the range resolution to calculate the range precision, which is the standard deviation of the  
115 range estimate for each reflector at the 68% confidence level, as per the following equation:

116 
$$\sigma(r^*) = \frac{\Delta r}{\sqrt{SNR}} \quad (S2)$$

117 This provides us with an estimate of the distance between the platform and a single  
118 reflecting target. SNR calculated for each IRH traced on the OIB-MCoRDS2 system at  
119 WD2014 varies between 6.54 and 7.68 dB. Using Equation (S2), this results in a maximum  
120 range precision  $\sigma(r^*) = 1.01 \text{ m}$ . As per Ashmore et al. (2020), we do not estimate SNR  
121 directly for PASIN and use a realistic range accuracy of  $\pm 4 \text{ m}$  to calculate our radar depth  
122 uncertainties. This is estimated by comparing the range resolution of the University of Texas's  
123 HiCARS system, which has a slightly higher range resolution (8.6 m) compared with PASIN  
124 (12.9 m; see Table 1 of the main manuscript) and for which radar range accuracy varies  
125 between 0.9 and 3.9 m over East Antarctica (Cavitte et al., 2016) (see Ashmore et al., 2020 for  
126 more details). Considering the chirped version of the radar system flown over Institute and  
127 Möller Ice Streams has the same centre frequency and a similar bandwidth to the Pine Island  
128 Glacier survey (2010 IMAFI-PASIN: 12 MHz, 2004 PIG-PASIN: 10 MHz), we estimate that  
129 using the same conservative value of  $\pm 4 \text{ m}$  for the range precision is appropriate here. Final  
130 range precision numbers and total uncertainties can be found in sections 2.3 and 2.4 of the main  
131 manuscript.

132

### 133 **Text S2: Age-depth Modelling Calculations**

134

135 We provide below additional information on the processing chain used to obtain the  
136 accumulation estimates over Site A-B and the WD2014 site, as well as the scientific rationale  
137 behind selecting a range of basal shear layer thickness ( $h$ ) scenarios for input into the 1-D  
138 model.

139

140 Firstly, a profile from the 1974-75 Scott Polar Research Institute/National Science  
141 Foundation/Technical University of Denmark (SPRI/NSF/TUD) survey, with IRHs traced and  
142 dated (Siegert and Payne, 2004) at their intersection with the Byrd Ice Core chronology  
143 (Hammer et al., 1997), crosses our profiles and extends into Thwaites Glacier and the upper  
144 Siple Coast catchments. At three crossovers (marked on Figure 1) where our R1-3 are traced  
145 in the PIG-PASIN profiles, we used the age-depth profile of Siegert and Payne (2004) to assign  
146 broad ages to our upper three IRHs. Table S3 shows the close correspondence between our  
147 traced IRHs and those from Siegert and Payne (2004) at Intersections 1-3. Acknowledging the  
148 spatial uncertainties associated with pre-GPS navigation in the SPRI/NSF/TUD records  
149 (Schroeder et al., 2019), we treated these as initial constraints to refine the input parameters of  
150 the age-depth modelling we describe in Section 2.4.2.

151

152 **Table S3.** IRH depths (m) at three locations where the SPRI/NSF/TUD survey intersects the PIG-PASIN survey.  
 153 The intersections mentioned here are shown as black arrows in Figure 1. Age and uncertainty for each of Siegert  
 154 and Payne’s (2004) IRHs is also shown here. The maximum depth uncertainty associated with our IRHs at a  
 155 catchment-scale is  $\pm 17$  m on PIG-PASIN (see 2.3). The uncertainty associated with Siegert and Payne’s (2004)  
 156 IRHs is  $\pm 40$  m.

	IRH depths at Intersections 1-3					
	<i>This study</i>			<i>Siegert and Payne (2004)</i>		
	R1	R2	R3	L07 ( $3.10 \pm 0.16$ ka)	L10 ( $5.60 \pm 0.18$ ka)	L11 ( $6.40 \pm 0.18$ ka)
I1	520.8	882.3	1146.0	500.8	896.7	1056.8
I2	508.4	975.0	1478.8	531.3	1034.4	1222.9
I3	569.6	999.6	1475.3	557.0	1055.5	1193.4

158  
 159 Secondly, the area covered by the Medley et al.’s (2014) snow accumulation product  
 160 does not extend to the WD2014 site. To solve this issue, we use data from a 7-MHz ground  
 161 penetrating radar driven in 2002-04 over the Western divide (Neuman et al., 2008) to  
 162 reconstruct accumulation rates across the divide and connect this to the Medley et al. (2014)  
 163 product. We merge both data sets together to provide one product, referred in the main text as  
 164 MED14. To ensure consistency across all observational and modelled products, and capture  
 165 intra-cell variability in accumulation rates, we bilinearly interpolate the resolution of the MAR  
 166 ( $35 \times 35$  km), RACMO2 ( $27 \times 27$  km), and ART06 ( $100 \times 100$  km) products to match the 3-  
 167 km resolution of MED14. We then take the closest grid value that corresponds to WD2014 and  
 168 each of Site A and B and convert the accumulation value from  $\text{kg m}^{-2} \text{a}^{-1}$  to  $\text{m a}^{-1}$  of ice-  
 169 equivalent using an ice density value of  $917 \text{ kg m}^{-3}$ .

170  
 171 **Table S4.** Accumulation rates ( $\text{m a}^{-1}$ ) for each IRH at Site A and B, as calculated using the four accumulation  
 172 datasets mentioned in the main text (see 2.4.2). Note that at Site B, R4 was not retrieved. The accumulation rate  
 173 is given in  $\text{m a}^{-1}$  (meters of ice equivalent per year) using an ice density value of  $917 \text{ kg m}^{-3}$ .  $\Delta \%$  refers to the  
 174 percentage change in accumulation rates between the WD2014 site and Site A and B respectively.

	<i>Site A</i>					<i>Site B</i>			
	R1	R2	R3	R4	$\Delta \%$	R1	R2	R3	$\Delta \%$
MAR	0.253	0.255	0.249	0.210	2.659	0.266	0.268	0.261	7.742
ART06	0.268	0.270	0.264	0.223	8.817	0.276	0.278	0.271	11.831
RACMO2	0.305	0.307	0.300	0.253	23.560	0.331	0.333	0.326	34.200
MED14	0.311	0.314	0.307	0.259	26.308	0.325	0.325	0.318	30.888

176  
 177 Thirdly, recent evidence suggests that the nearby Amundsen-Weddell divide has been  
 178 relatively stable throughout the Holocene and further back in time (Hein et al., 2016; Ross et  
 179 al., 2011), although it has been suggested that the neighbouring Amundsen-Ross divide is  
 180 currently migrating toward the Siple Coast at a rate of  $10 \text{ m a}^{-1}$ , mainly driven by ice dynamics  
 181 over the last  $\sim 2000$  years (Conway and Rasmussen, 2009; Neuman et al., 2008). Moreover,  
 182 elevated geothermal heat flux around the Western divide suggests relatively high basal melting  
 183 rates in the area (Fudge et al., 2019). Considering that the vertical velocity profile under  
 184 present-day conditions is dependent on a good approximation of the flow and bed conditions  
 185 at the divide, Neuman et al. (2008) tested two scenarios to estimate the basal shear layer  
 186 thickness over the Western Divide. The parametrisation of their model used both  $h = 0.2H$   
 187 (corresponding to a divide where basal sliding or divide migration is occurring) and  $h = 0.7H$   
 188 (representing a stable divide with frozen bed). They show that values where  $h > 0.2H$  required  
 189 increasingly more accumulation at the divide to match the age of the radar-detected IRHs dated

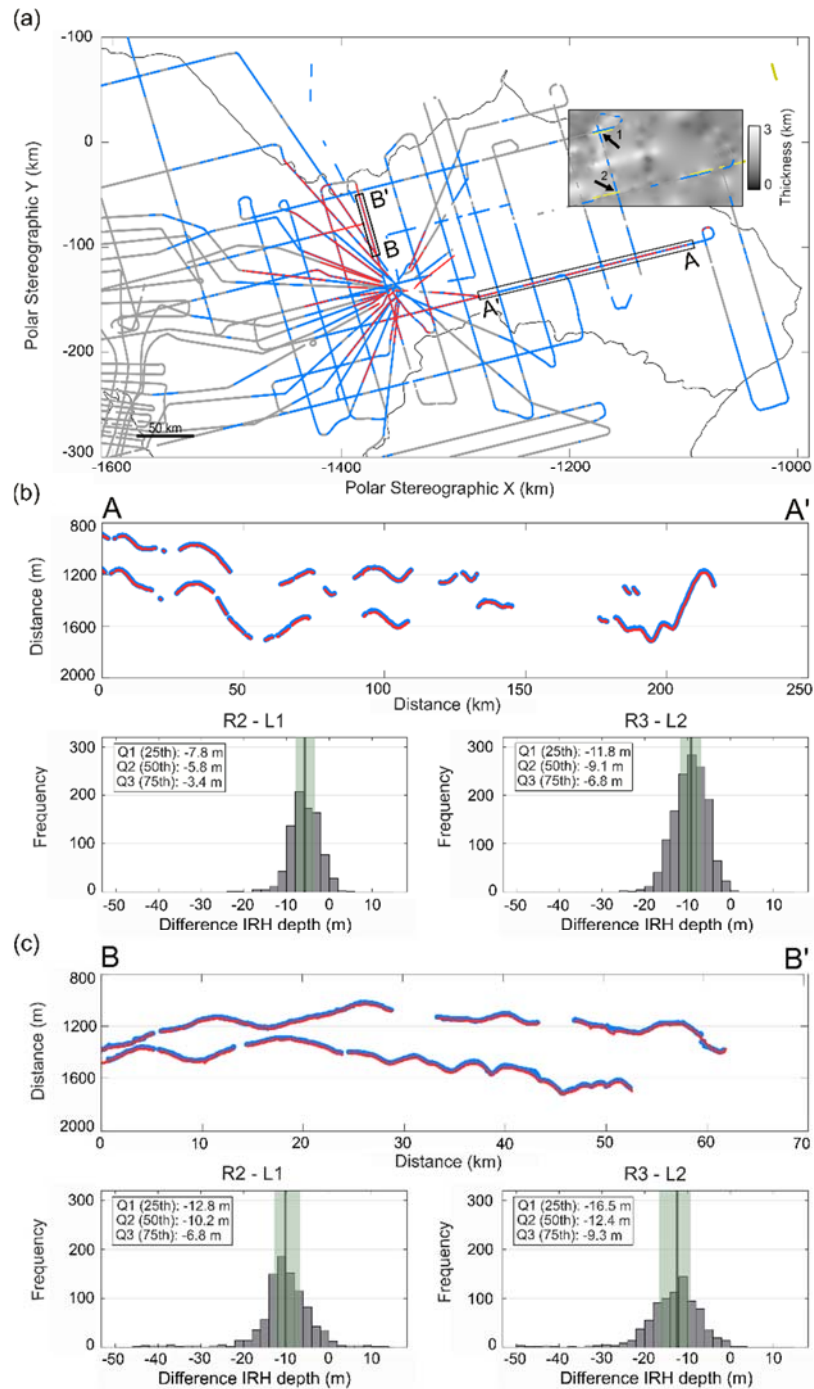
190 at Byrd ice core. Schwander et al. (2001) used  $h = 0.373H$  at Dome Concordia (East  
191 Antarctica), but accumulation is lower there than at the WAIS Divide and ice flow has likely  
192 changed little since the last interglacial. Owing to the above, and considering that ice thickness  
193 at Site A is  $H = 3605\text{ m}$  and at Site B is  $H = 3430\text{ m}$  ( $\pm 23\text{ m}$ ; Vaughan et al., 2006), using  
194 a range of values for  $h$  of 100–1200 m as per Ashmore et al. (2020) and Karlsson et al. (2014)  
195 is not appropriate here. We therefore refine this range to between  $0.2H \leq h \leq 0.3H$ . We note,  
196 however, that large uncertainties in basal deformation at WD2014 (Cuffey et al., 2016; Fudge  
197 et al., 2019) could result in  $h$  values being smaller than 20% of the ice thickness and thus lead  
198 to an overestimation of our ages. Values for  $h$  are provided in Section 2.4.2 and in Table 4 of  
199 the main text.

200

201 **Additional Figures:**

202

203

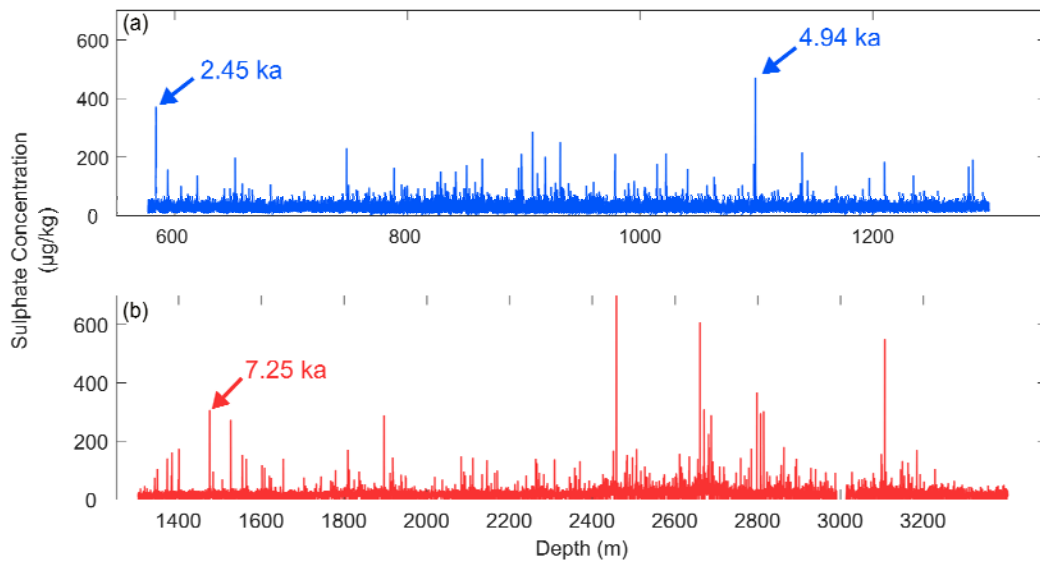


204

205

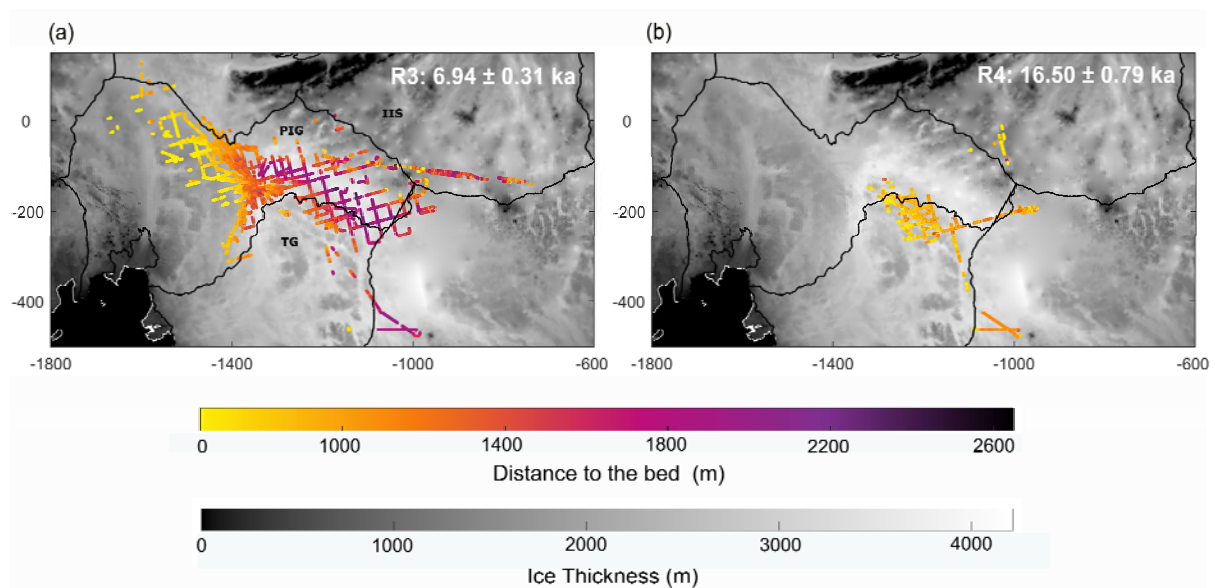
206 **Figure S3.** Comparison between our IRHs and Karlsson et al. (2014) and Ashmore et al.'s (2020) IRHs. (a) Spatial  
 207 extent of traced IRHs over Pine Island Glacier using the PIG-PASIN dataset: subset of R2-3 package from this  
 208 study (blue), Karlsson et al.'s (2014) Layer 1-2 (abbreviated in the figure as L1-2) (red). The grey lines in the  
 209 background show a subset of the PIG-PASIN flight lines onto which Karlsson et al.'s (2014) Layer 1-2 were  
 210 traced. The black outline lines are the ICESat IMBIE basins containing the Pine Island and Thwaites glaciers  
 211 (Zwally et al., 2012). Inset in top right shows the location where Ashmore et al.'s (2020) H2-3 (yellow) from the  
 212 PIG-PASIN survey (see Figure 1 in main text) intersect our IRHs over PIG, with ice thickness (m) from  
 213 BedMachine (Morlighem et al., 2020) in the background. The black arrows are where we directly compare  
 214 Ashmore et al.'s (2020) H2 and our R2. (b) Comparison between R2-3 (blue) and Karlsson et al.'s (2014) L1-2  
 215 (red) (top) and histograms showing the key statistics of the difference between R2/L1 and R3/L2 (bottom) for  
 216 segment A-A' (see (a)). The median is represented by the thick green line and the 25<sup>th</sup> and 75<sup>th</sup> interquartile range  
 217 is shown in shaded green. (c) As (b) but for segment B-B'. Note that the segments A-A' and B-B' shown here are  
 218 distinct from the AA-AB segment shown in Figure 1 of the main manuscript.

219



220  
 221  
 222  
 223  
 224  
 225  
 226

**Figure S4.** Sulphate concentration ( $\mu\text{g}/\text{kg}$ ) as a function of depth (m) at the WAIS Divide ice-core site for: (a) the brittle section of the WDC06A ice core (577-1300 m) from Cole-Dai (2014); and (b) for depths of 1300-3404 m at WD2014 ice core from McConnell (2017). Peaks of sulphate concentration matching the age-depths of R1-3 and dated at 2.45 ka, 4.94 ka, and 7.25 ka are also shown. The ages shown are from the WD2014 chronology and are in years before 2020 AD.



227  
 228  
 229  
 230  
 231  
 232  
 233  
 234

**Figure S5.** Ice thickness (m) below R3 (a) and R4 (b) traced over the PIG-PASIN and OIB-MCoRDS2 data. The ages are from the intersection with the WD2014 ice-core site (see Table 3 in the main text). Background is ice thickness in meters from BedMachine (Morlighem et al., 2020). The white line is the Antarctic coast line and the black outlines are the ICESat IMBIE basins containing the Pine Island Glacier, Thwaites Glacier and the Institute Ice Stream (Zwally et al., 2012). The abbreviations in (a) are as follows: PIG (Pine Island Glacier), TG (Thwaites Glacier), IIS (Institute Ice Stream).